UNIVERSITÀ DEGLI STUDI DI BERGAMO
SCHOOL OF ENGINEERING
DEPARTMENT OF ENGINEERING AND APPLIED SCIENCES
DOCTORAL PROGRAMME IN ENGINEERING AND APPLIED SCIENCES

"EXPERIMENTAL AND NUMERICAL INVESTIGATION OF FILM COOLING JET ON A FLAT PLATE WIND TUNNEL"

Doctoral Dissertation of:
SAMANEH ROUINA

Supervisor:
Prof. Antonio Perdichizzi

Tutor:
Prof. Giovanna Barigozzi

The chair of doctoral Program:
Prof. Valerio Re

Year 2017 - Cycle XXX

ABSTRACT

An experimental and numerical study was conducted to investigate the unsteady behavior of film cooling jet for two different hole geometries on a flat plate wind tunnel. The numerical part was devoted to the assessment of different turbulence models to get the best prediction of both aerodynamic and thermal performance with a conventional RANS approach. The investigated hole geometries include a row of three cylindrical holes and a row of three fan-shaped holes with an inclination of 30 degrees with respect to the flat plate. Tests have been carried out at low speed and low inlet turbulence intensity level, with blowing ratios varied in the range of 0.5–1.5, and 1-2 for cylindrical and fan-shaped holes, respectively. Aerodynamic investigations have been performed by means of Laser Doppler Velocimetry (LDV), Particle Image Velocimetry (PIV), and Hotwire Anemometry (HW). LDV was used to study the boundary layer behavior just downstream of the holes. A high- resolution PIV system was used for flow visualization and flow field measurement to investigate the unsteady mixing process taking place between the coolant and main flow. Furthermore, HW has been used to measure velocity components in a vertical-lateral plane. For thermal measurements, the binary PSP technique was used to measure adiabatic film cooling effectiveness. Results obtained from aerothermal experiments show that by expanding the exit of the cooling hole, the penetration of the cooling jet is significantly reduced relative to the cylindrical hole, thereby providing a better coverage over the flat plate even at high blowing ratios. Furthermore, the effect of density ratio was investigated using CO_2 as a foreign gas. In the same BR, the jet with a greater density ratio provides better film protection over the flat plate surface. Finally, detailed experimental data was compared with three turbulence models, which are RKE, SST KW and RSM turbulence models, in the state-of-art CFD code STAR-CCM+, result in selecting SST KW and RSM turbulence models for cylindrical and fan-shaped holes, respectively.

Acknowledgement

This thesis represents not only my work at the keyboard, it is the result of efforts and supports of many other individuals at turbomachinery lab of university of Bergamo, the so-called **LABMAC**. My experience at LABMAC has been nothing short of amazing, and since my first day on February 2nd, 2015 I have felt at home there. I have been given unique opportunities which included working with the cutting edge equipment in a research-based environment with a group of talented and experienced individuals who I wish to acknowledge. First and foremost I wish to thank my advisor, Professor **Giovanna Barigozzi**, who has been supportive and dedicated both academically and emotionally through the rough road to finish this thesis. Thanks to her I had the opportunity to modify the test set-up, and perform a lot of different kind of tests, she helped me with elaboration and analysis of data and guided me in every steps of my works even during the most difficult times such as writing this thesis, providing me with priceless insights. Thank you to Professor **Silvia Ravelli** who guided me through simulation part of my work, thank you for all the valuable comments that you shared with me. My great thanks goes to Professor **Antonio Perdichizzi**, none of these would have happened without his support. Besides my advisors, I would like to thank my thesis referees, Professor **Franco Rispoli**, and Professor **Carlo Carcasci** for their insightful comments which enhance the quality of this thesis.

Thank you to my lab mates who have helped me immensely during these years: **Paolo**, **Luca**, **Mairo**, **Silvia**, **Ettore**, **Victor**, **Simone**. Thanks for being true friends to me and welcomed me to the new environment with open arms. I have learned a lot from you guys. Also thank you to **Matteo**, the graduate student, who have helped me during most part of data acquisition. He had been amazing help all this time. A special group from the LABMAC is not mentioned yet, because they deserve their own part: **Dean Enzo and Fabio**,

our laboratory technicians. I appreciate their enormous amount of help for preparation of test set-up.

Thank you to my special lab mate, best friend, and husband, **Hamed**, who is always an inspiration to me. You are the one who has always been there for me since 8 years ago and always encourage me to be a better version of myself.

Last but not the least, I would like to thank my parents and my sisters who are the source of energy and unconditional love. They teach me to never give up and the importance of persistence and effort in life. Thank you for believing in me and sacrificing a lot for me through this long road.

Table of Contents

List of Figures

List of Tables

Preface

Energy is an integral part of human day-to-day life, and exploitation of fossil fuels resources put human in an energy crisis danger. The answer to fix this problem is using alternative energies or increasing the performance of available systems. Nowadays, gas turbines are one of the most widely-used power generating technologies. The focus of this thesis is to investigate one of the crucial aspect that influences the performance of gas turbines: Film cooling. Efficient film cooling increases gas-turbine performance, thereby decreasing the fuel consumption.

1

INTRODUCTION TO FILM COOLING IN GAS TURBINE

Gas turbines are widely used in many fields of engineering such as aircraft propulsion and in land-based power generation (Fig. 1-1). The main components of the gas turbine engine are the compressor, combustion chamber and turbine and a simple gas turbine cycle consisting of these elements is shown diagrammatically in Figure 1-2. The ideal cycle for gas turbine work is the *Brayton Cycle* (Fig. 1-3). The gas is compressed from state point 1 to 2 through the compressor, and energy is added to the flow in the form of heat by the burning of fuel in the combustion chamber between state points 2 and 3 along an isobaric line. The high pressure and high enthalpy flow is then expanded through the turbine, which produces shaft work that drives the compressor, and extra useful power output that is used to provide propulsion in the aero jet engine by producing thrust due to the jet created in the propelling nozzle or shaft work from extra turbine stages for the industrial gas turbine [1].

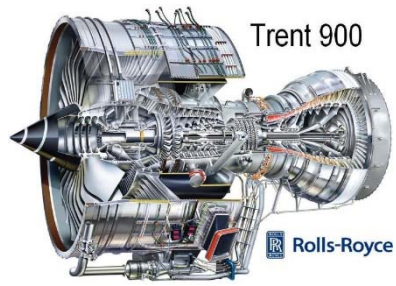

Fig. 1-1. Rolls-Royce Trent 900.

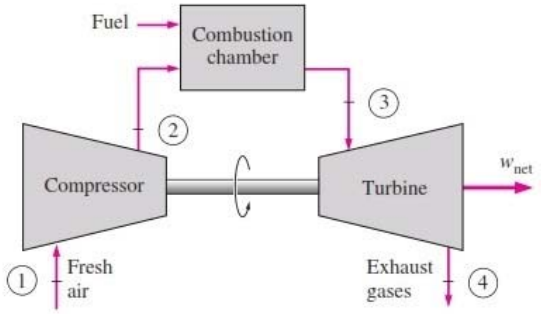

Fig. 1-2. Diagram of a simple gas turbine system.

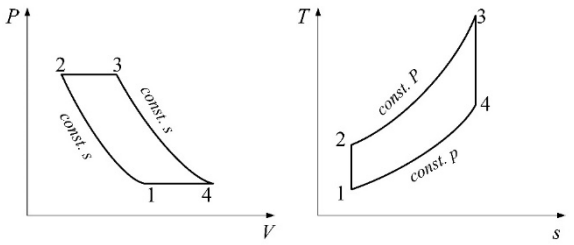

Fig. 1-3. P-V and T-s diagrams of an ideal Bryton cycle.

Thermal efficiency and power output of gas turbine increase with increment in turbine inlet temperature (TIT) which is illustrated in figure 1-4. Clearly, to double the engine power in aircraft gas turbine, the TIT should increase from 2500°C to 3500°C which is well above the turbine blade and vane operating metal temperatures. To reach this goal, two important issues should be addressed; high-temperature material development and the use of thermal barrier coating (TBC) and more significantly film cooling technologies which aim to protect the material from extreme temperature [2].

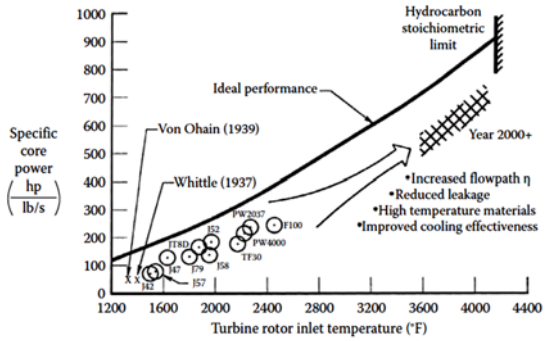

Fig. 1-4. Increasing inlet temperature dramatically improves cycle power output; Sautner et al. [3] (courtesy of Pratt &Whitney)

Turbine cooling design aims to provide a relatively uniform material temperature within the material operating temperature limit in order to minimize thermal stress and maximize component life.

1.1 Turbine Cooling Technology

Advanced cooling technologies classified into blade internal cooling (fig. 1-5(b)) and external cooling (fig. 1-5(a)). Internal cooling is achieved by passing the coolant through several passages inside the blades and extracting the heat from the outside of the blades. External cooling is also called film cooling. Internal coolant air is ejected out through discrete holes or slots to provide a coolant film to protect the outside surface of the blade from hot combustion gases [2].

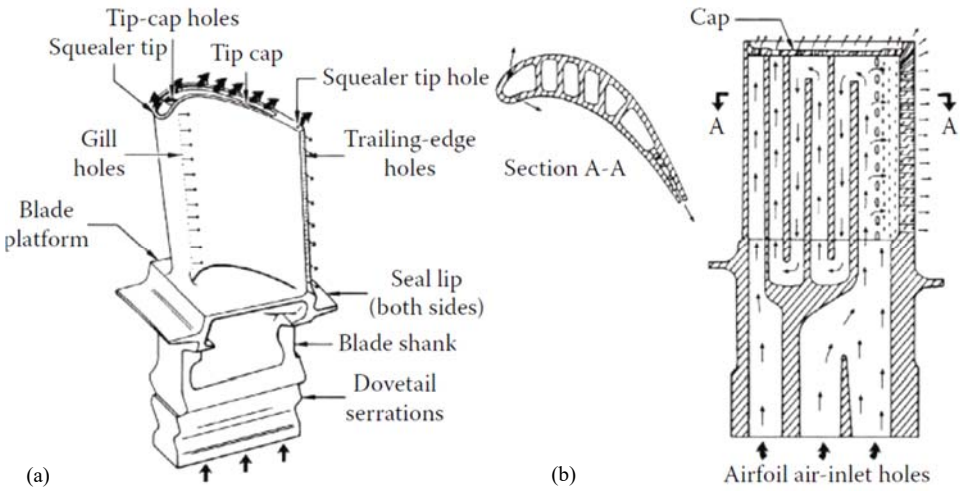

Fig. 1-5. Gas blade cooling schematic (a) External cooling (b) Internal cooling.

Highly sophisticated cooling techniques in advanced gas turbine engines include film cooling, impingement cooling, and augmented convective cooling. For example, figure 1-6 shows complicated internal impingement cooling and external film cooling geometry of a state of the art GE CF6 turbofan engine nozzle guide vane (NGV).

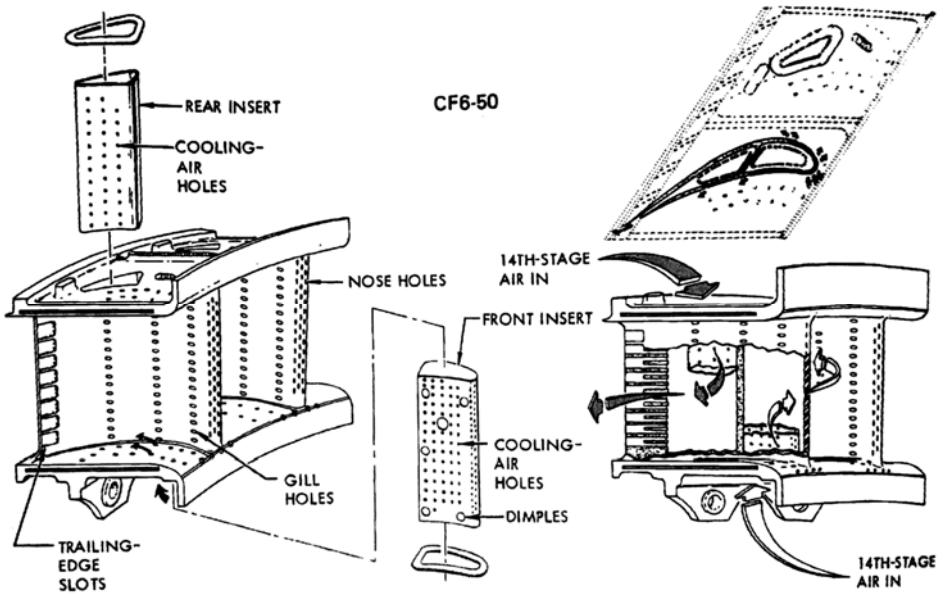

Fig. 1-6. First stage high pressure turbine nozzle vane for the GE CF6 engine [4].

Air used for cooling is drawn from the outlet of the compressor, resulting in losses in overall engine efficiency due to the loss of work producing capacity, in addition to thermodynamic and aerodynamic losses due to the mixing of coolant air with hot mainstream flow. Therefore, a thorough understanding of the flow-field and thermal aspects of film cooling jet and crucial parameters that affect film cooling performance is of great value to the engine designer.

1.2 Film Cooling

In film cooling, jets of relatively cooled air are ejected through rows of holes in the blade surface to form a protective layer between the surface and hot mainstream gas. A typical example of this is presented in Figure 1-7 [5].

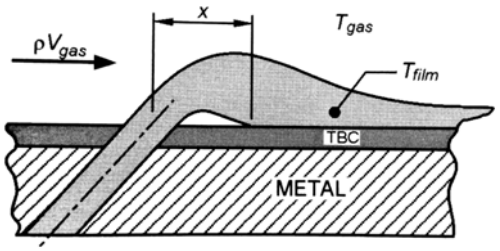

Fig. 1-7. Film Cooling Effectiveness

Film cooling protection is provided by the reduction in heat flux between the mainstream and the surface and by the coolant absorbing some of the heat from the mainstream gas. For constant property flows, the heat transfer between the layer and the blade surface can be written as [6]:

$$q = h(T_f - T_w) \qquad \textit{Equation 1-1}$$

Where h is heat transfer coefficient, T_f is film cooling temperature, and T_w is blade surface temperature. As the cooling film interacts with the mainstream film, its performance is defined by a parameter known as adiabatic film-cooling effectiveness which is calculated as follows:

$$\eta = \frac{T_\infty - T_{aw}}{T_\infty - T_C} \qquad \textit{Equation 1-2}$$

Where η is the film cooling effectiveness, T_{aw} is the adiabatic wall temperature; T_∞ is the temperature of the hot gas, and T_c is the temperature of the injected coolant.

1.3 Film Cooling Physic

Resulting cooling jet flow structures and its performance are dependent on a large number of parameters, including:

- ✓ Film cooling hole geometry: affecting parameters include hole diameter (D), the inclination of the film-cooling hole with respect the surface to be cooled (α), Hole pitch (P), film-cooling hole length to diameter ratio (L/D) as shown in figure 1-8.

- ✓ Properties of the coolant and mainstream: A common modeling parameter for this flow feature is the density ratio which is defined as the ratio of coolant density with respect to mainstream density:

$$DR = \frac{\rho_c}{\rho_\infty} \qquad \textit{Equation 1-3}$$

- ✓ Mainstream turbulence intensity (Tu) which is calculated as:

$$Tu = \frac{\sqrt{\frac{1}{3}(u'^2 + v'^2 + w'^2)}}{U} \qquad \textit{Equation 1-4}$$

Where u', v', and w' are root-mean-square (rms) velocity components and U is the mainstream velocity.

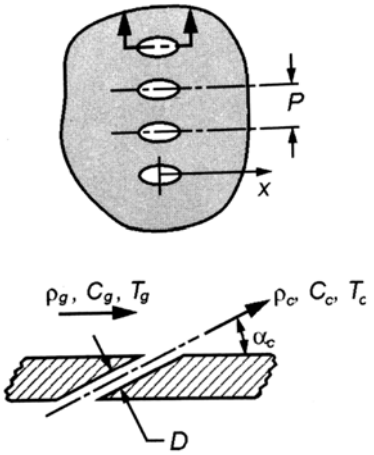

Fig. 1-8. Film cooling parameters [5].

- ✓ Blowing Ratio which defines as coolant-to-mainstream mass flux ratio and calculates as follows:

$$BR = \frac{\rho_C u_c}{\rho_\infty u_\infty} \qquad \textit{Equation 1-5}$$

- ✓ Momentum flux ratio is the Momentum flux of film cooling flow, versus momentum flux of mainstream which could be written as follows:

$$I = \frac{\rho_C u_C^2}{\rho_\infty u_\infty^2} \qquad \textit{Equation 1-6}$$

- ✓ Mainstream boundary layer thickness to film-cooling hole diameter ratio ($^{\delta}/_{D}$)

The effect of all above-mentioned parameters on film cooling behavior are described in detail in next chapter

2 Literature survey

As well known, turbine inlet temperature is the driving parameter to improve gas turbine performance. Hot components in modern gas turbine engines work at temperature levels well above the limit imposed by technological constraints. As a result, the efficient cooling system is required to ensure that turbine vanes and blades withstand such high thermal loads. In modern gas turbine, film cooling is extensively used, together with internal cooling, to cool all the exposed surfaces, i.e. vanes, rotor blades, and platform. Film cooling not only determines the heat exchange characteristics of the airfoils, but also affects its aerodynamic performance. The main effects are on the one hand a reduction of the adiabatic wall temperature and on the other the aerodynamic mixing between main and coolant flow, which results in a general increase of losses with a consequent decrease in the aerodynamic efficiency of the component. The injection of a jet in the main flow, in fact, implies the establishment of a three-dimensional flow, in which counter-rotating vortices, the so-called kidney vortex pair, appear [2]. These vortices are responsible for the entrainment of hot main flow towards the wall, resulting in a decrease of thermal protection. So, accurate information on the interaction of coolant injection with boundary layers developing on the airfoils is required to optimize the cooling design from the aerodynamic and thermal point of view.

Over the years, vast numbers of investigation have been carried out regarding the parameters effecting film cooling. It has been found that film cooling is very sensitive to hole geometry, the coolant to mainstream density, momentum and mass flux ratios, the mainstream turbulence intensity and so on. Thorough reviews of these parameters are provided by Goldstein [6], Han et al. [2], Han and Ekkad [7], Bogard and Thole [8], and Bunker [9].

On the other hand, recent advances in turbulence modeling have allowed for an accuracy of numerical prediction of film cooling behavior. Several recent works have used in-house and commercial CFD codes to predict film cooling behavior successfully, using RANS as well as LES approaches [22-33].

In the following chapter, experimental and numerical investigations concerning film cooling on the flat plate that have been done in literature are reviewed. It is common in the literature to use a flat plate to investigate film cooling behavior since it is a simple geometry and results obtained on a flat plate could be later used to calibrate various experimental techniques to drive correlations for the prediction of η, h which are useful in the first step of the design process.

2.1 Flat plate film cooling-Experimental Studies

In this section, a brief review of various parameters on film cooling will be presented.

Effect of Hole Configuration

The geometry of the film cooling hole has a profound impact on the coverage of the film. Film cooling holes with low injection angles provide a better coverage in the downstream region when compared with 90° injection since coolant remains attached to the surface over a greater distance. Compound angle configurations are also found to resist to lift-off more than simple angled

configuration [10]. The same beneficial effect can be obtained by shaping the hole exit section. Adding a diffusion section at the hole exit, in fact, reduces the jet momentum, allowing it to stay closer to the wall, in the meanwhile distributing the coolant over a wider region [11]. In addition, many studies have shown that length-to-diameter ratio (L/D) significantly influences the hole-exit velocity profiles and the interaction between coolant jet and mainstream. Longer holes allow the coolant flow to become fully developed which leads to improvement in film cooling performance [12].

Effect of Coolant-Mainstream Blowing Ratio

Blowing ratio (BR) is defined as the ratio of the coolant mass flux to that of the mainstream. The amount of coolant flowing through the hole affects how the coolant interacts with the mainstream, and therefore, optimizing the blowing ratio is critical because blowing rates that are too high lose more coolant into the mainstream due to phenomenon of film-cooling lift-off, whereas low blowing ratios do not provide enough coolant to effectively cover the surface [13].

Effect of Coolant-Mainstream Density Ratio

In modern gas turbine engine, the coolant to mainstream density ratio (DR) is usually around 2.0. Laboratories, to simulate engine DR condition, usually chill the coolant to very low temperatures [14] or make use of a foreign gas with a higher density such as Carbon Dioxide [15]. Generally, increasing density ratio at a certain blowing ratio results in a higher effectiveness, especially at higher blowing ratios, since the momentum of high-density coolant is lower at a given BR, thus reducing the tendency to lift-off.

Multiple Row Film Cooling

Multiple rows of film cooling holes with diverse injection direction (i.e. backward and forward injection) are common in turbine blade design. Ligrani et al. [16] investigated the heat transfer and adiabatic film cooling effectiveness

of two staggered rows of cylindrical holes. At low blowing ratios, numbers of rows did not result in significantly higher effectiveness. However, the double jet row showed higher effectiveness at high blowing ratio. Ahn et al. [17] conducted an experiment using rows of film cooling holes with opposite orientation angles. The TLC measurement showed improvement in film cooling effectiveness due to the fact that film cooling jets of inline configuration were attached to the surface not lifted off at high blowing ratio.

More recently, Kusterer et al. [18] studied two rows of film cooling holes with opposite orientation which resulted in higher film cooling effectiveness by canceling out the counter-rotating kidney vortices.

Effect of Mainstream Turbulence

Another important factor influencing the coolant coverage is the turbulence intensity of the mainstream flow which its value depends on the location. The turbulence intensity at the exit of the combustor can be as high as 20%, and at the rotor inlet, the intensity can be in the range 6-12% [19]. For inclined cylindrical holes, increasing the turbulence intensity decreases the centerline film cooling effectiveness at low blowing ratios. However, at high blowing ratios, the increased turbulence increases the centerline effectiveness as the penetration of the coolant into the mainstream is reduced [20].

2.2 Flat plate film cooling-Numerical Studies

Several CFD studies on film cooling are available in the literature. Computational methods that could be adopted for the analysis of film cooling are direct numerical simulation (DNS), large eddy simulation (LES), simulation based on Reynolds Average Navier Stokes (RANS) and detached eddy simulation (DES). Among these methods, DNS and LES have the highest potential to provide reliable results. Meanwhile, RANS simulation has an advantage in short turn-around time suitable for designing usage. Figure 2-1

compares the number of grid points required for each simulation [21]. RANS simulation requires a smaller number of grid points than those required in DNS and LES.

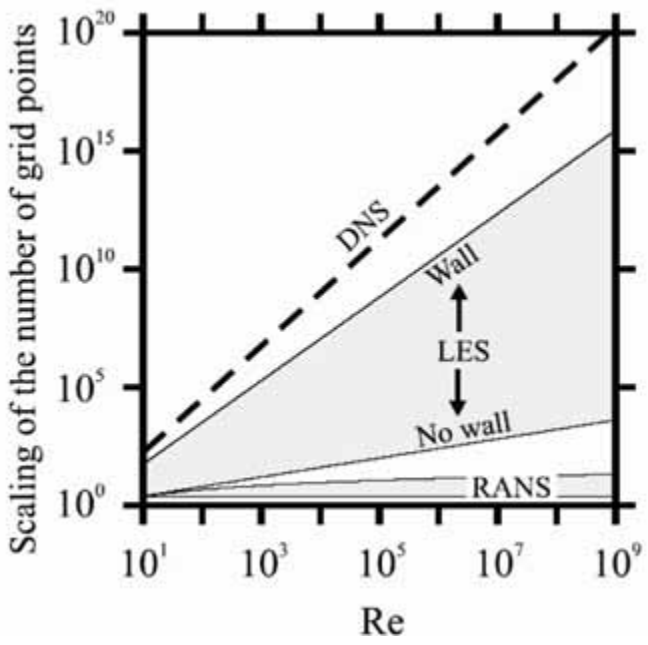

Fig. 2-1. Relationship between the number of grid points and Re

A number of RANS simulation have been carried out on film cooling flow fields on a flat plate. Walters and Leylek [22] developed a systematic computational methodology for film cooling CFD simulation. Their methodology addressed four critical issues in a computational simulation: a computational model of the physical problem, geometry and grid generation, discretization scheme, and turbulence models. They simulated adiabatic effectiveness using the standard k-ε (SKE) with standard wall function (SW) and compared it to data from Sinha et al. [14]. Downstream of the film hole, computational results tended to show higher centerline effectiveness values, yet laterally-averaged effectiveness was in good agreement with the experimental result.

The Walter and Leylek group later studied seven different turbulence models. SKE with two-layer wall treatment (2LWT) predicted experimental measurements of centerline effectiveness by Sinha et al. [14] more accurately than renormalization group k-ε (RNG) or Reynold's stress models (RSM) at BR=1 [23,24].

Javadi et al. [25] simulated normal jet film cooling injection using shear stress transport (SST), SKE with 2LWT, and RSM with 2LWT. The RSM best predicted jet velocity profiles, shear stress and turbulence kinetic energy found by Ajersch et al. [26] at various blowing ratio.

In another study, York and Leylek [27] compared SKE and realizable k-ε (RKE) turbulence models with 2LWT simulating turbine vane and found the RKE better matched experimental data by Hylton et al. [28] than the SKE. Silieti et al. [29] investigated flat plate film cooling using SKE, RNG, RKE, standard k-ω (SKW) and SST turbulence models. The study found that downstream of the hole ($x/d<6$), the RKE model best predicted experimental centerline η data from Gritsch et al. [10] for BR=1. Farther from the hole ($6<x/d<10$), the SKE model predicted the experimental data most accurately. The RNG, SKW, and SST models under-predict centerline η near the hole and over-predicted η farther from the hole.

Hassan and Yavuzkurt [30] examined capabilities of SKE, RNG, RKE, SKW turbulence models in predicting film cooling effectiveness under high free stream turbulence (FST) intensity (Tu=10%). At low blowing ratio (BR=0.5), best results for effectiveness were obtained with SKE model. At high blowing ratio (BR=1.5), the SKE and SKW models result for effectiveness were similar but consistently high with respect to the data even though the trends were similar. The RNG and RKE models results were closer to the data but trends were completely different.

Gustafsson and Johansson [31] used the RKE, SST, and RSM turbulence models with considering 2LWT for all three cases and compared the velocity profiles to experimental data also presented in the paper. They found that the RSM model predicted experimental results more accurately than two other turbulence models.

Harrison and Bogard [32] have examined the effects of various turbulence models by comparing not only laterally averaged, centerline, and lateral distributions but also they included heat transfer coefficient augmentation comparison to their work. They found that the SKW model best predicted laterally-averaged adiabatic effectiveness and the RKE models resulted in the worst predictions. Centerline adiabatic effectiveness was best predicted by the RKE model and the worst predicted by the SKW. All turbulence models provide poor predictions of lateral distributions due to lack of sufficient lateral spreading. Even using the RSM (Reynold's stress) model, simulations did not result in significantly better lateral spreading. However, they picked SKW the best model considering predicting laterally averaged adiabatic effectiveness and heat transfer.

Silieti et al. investigated fan-shaped film cooling hole on a flat plate using the RKE, SST, and V2F turbulence models [33]. The RKE and SST models matched very well with centerline effectiveness near the hole, but SST model results agreed slightly better with experiments by Gritsch et al. [11] far from the hole.

2.3 Motivation of the present work

Based upon the open literature review, most of the experimental data available in the literature refer to averaged information, i.e. assume that the jet to mainstream mixing process can be considered as a steady problem. Recent studies have shown that jet to mainstream mixing process is, in fact, an unsteady and highly anisotropic phenomenon [34, 35]. The first objective of this work is

to characterize in detail the aerodynamic and thermal behavior of film cooling jet injected from two different hole geometries. A complete aero-thermal analysis has been obtained by means of velocity flow field measurements in different planes and by measuring adiabatic effectiveness. The aerodynamic flow field has been investigated by means of Particle Image Velocimetry (PIV) and hotwire anemometry (HWA) which provided detailed information about the unsteady behavior of the film cooling jet. Concerning the adiabatic effectiveness measurements, binary PSP technique was developed and validated by comparing to TLC measurements on the flat plate as well as with the literature.

The second objective of this thesis is to assess three turbulence models, which are RKE, Menter SST k-ω (SST KW)and RSM turbulence models, in the state-of-art CFD code STAR-CCM+ by means of detailed experimental data. It is difficult to determine the best turbulence model based on literature since the same turbulence model predict very different results in different commercial CFD codes. Therefore, the development and application of turbulent models rely on experimental data is an important task. Furthermore, many works considered cylindrical holes and there are few studies investigating fan-shaped holes numerically. Hence, the experimental database used to pick the best model for predicting the film cooling jet behavior injected from a fan-shaped hole.

It goes without saying that studies typically focus on the thermal aspect of film cooling by evaluation of η, and results on aerodynamic aspects are scarce. The original contribution of this work is the complete set of data collected on film cooling problem, that includes both points of view: thermal and aerodynamic.

3 Measurement Techniques

In the following chapter, measurement techniques that have been used in the present study for acquiring aerodynamic and thermal experimental data will be explained.

3.1 Laser Doppler Velocimetry

Laser Doppler Velocimetry (LDV) as shown in figure 3-1 is a technique used to measure the instantaneous velocity of a flow field. This technique, like PIV, is non-intrusive and can measure all the three velocity components. In this study, a 2D component Laser Doppler Velocimetry was used to study the boundary layer upstream (X/D = -7 from hole downstream edge) and just downstream of the holes (X/D = 1 and 5) for variable injection condition as shown in figure 3-2. In all cases, the measurement volume was located at mid hole centerline (Z/D = 0). The light source was a 300mW Ar^{+} laser. A 200 mm focal length front lens allowed to get a measurement volume 0.06 mm in diameter and 0.6 mm in length. Two Burst Spectrum Analyzers (DANTEC BSA) were used to process the signals coming from the photomultipliers. All measurements were carried out acquiring 20,000 burst signals at each location. The high number of acquired signals assured statistically accurate averages:

based on a 95% confidence level, uncertainties of ±0.41% and ±0.7% for mean and RMS values have been obtained, respectively.

Fig. 3-1. 2-D LDV System

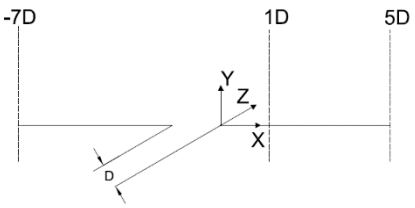

Fig. 3-2. LDV Measurement

3.2 Particle Image Velocimetry

It is evident today that the introduction of Particle Image Velocimetry in Fluid Mechanics is such a breakthrough. The PIV is a non-intrusive, whole field optical technology which provides accurate quantitative information on the instantaneous spatial structure of the flow. It is a unique means to capture vortices and coherent structures in unsteady regions of the flow [36].

Principles

In the following, the basic features of PIV measurement technique will be described briefly. Figure 3-3 sketches a typical setup for PIV recording in a wind tunnel. Small tracer particles are added to the flow. These particles are illuminated in a plane of the flow at least twice within a short time interval by laser. The light scattered by the particles is recorded either on a single frame or in a sequence of frames. The displacement of the particle images between the light pulses is determined through evaluation of the PIV recordings. In order to be able to handle the great amount of data which is collected employing the PIV technique, sophisticated post-processing is required [37].

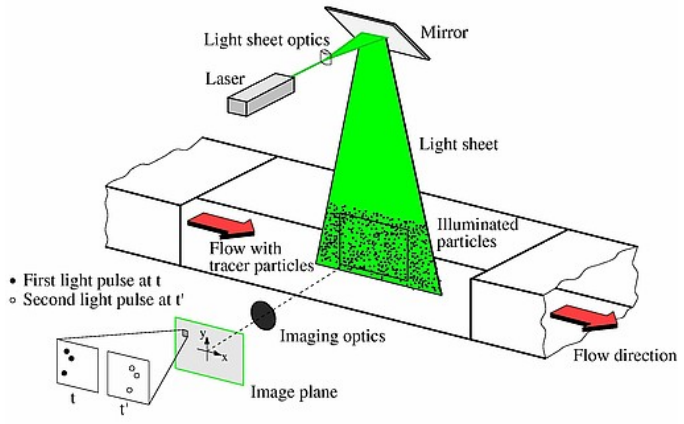

Figure. 3-3. Experimental arrangement for particle image velocimetry in a wind tunnel.

For evaluation, the digital PIV recording is divided into small subareas called “Interrogation areas”. The local displacement vector for the images of the tracer particles of the first and second illumination is determined for each interrogation area by means of statistical methods (auto- and cross-correlation).

It is assumed that all particles within one interrogation area have moved homogeneously between the two illuminations. The projection of the vector of the local flow velocity into the plane of the light sheet is calculated taking into account the time delay between the two illuminations and the magnification at imaging.

PIV Image Recording

In the following, some important factors regarding correct PIV image acquisition are reported.

First of all, choice of seeding particles with correct physical properties is an essential. Seeding particles should be able to follow the fluid in motion with minimum possible velocity lag. On the other hand, the particle size determines

the amount of the scattered light. The bigger is the diameter, the larger will be the amount of scattered light, yet the bigger particles have higher inertia to drift with respect to the fluid. Therefore, it is clear that a compromise has to be found.

Another crucial factor of PIV image recording is the light intensity of images which is proportional to light source intensity and exposure time for a certain *f*-number of the lenses. The exposure time has to be as short as possible in order to avoid blurring of the image.

To sum up, it should be mentioned that the separation time between pulses must be long enough to be able to determine the displacement between the images of the tracer particles with sufficient resolution.

PIV set up

Two sets of experiments have been done by means of the 2D-PIV system: flow visualizations and flow field measurements. Flow visualizations and flow field measurements were performed on streamwise plane located at the mid hole centerline (Z/D = 0). Also, flow visualization was conducted from the top of the wind tunnel (Y/D = 0.5).

Illumination was provided by a double-pulsed Nd: YAG laser emitting two pulses of 200 mJ at the wavelength of 532 nm with a repetition rate of 10 Hz. A CCD camera with a resolution of 2048 x 2048 pixels equipped with Nikkor lenses was used to capture images. The CCD camera and the double-pulsed Nd: YAG lasers were connected to a workstation (host computer) via a timer box which controlled the timing of the laser illumination and the image acquisition. Moreover, the data captured by the CCD camera was post-processed using Dantec software. Flow field measurements have been conducted in three steps: calibration, measurement, and post-processing. A checkerboard target with a spacing of 5mm x 5 mm was used to perform calibration. For each blowing ratio, 200 image pairs were recorded, and each pair of images post processed

using Adaptive PIV with minimum interrogation area of 32×32 pixels and 50% overlap.

For flow field visualization only the coolant flow was seeded by means of a Laskin seeding generator making use of vegetable oil. On the other hand, for velocity flow field measurements (LDV and PIV) also mainstream was seeded by SAFEX fog generator. The measurement uncertainty level for the velocity vectors is estimated to be within 2%.

3.3 Hotwire Technique

Hotwire anemometry (HWA) has been used for many years to measure velocity fluctuations in turbulent flows. It is well suited for turbulent flow studies in low Reynolds number air/gas flows with low to moderate turbulent intensities (<25%). HWA is relatively easy to use, provides a continuous analog output, meaning no information is lost and has an excellent temporal resolution for spectral measurements.

Within the last decade, research on hotwire anemometry has included studies on data reduction methods [38], improving measurement accuracy [39] calibrating with different fluid properties [40], and measurement techniques [41], [42]. In principle, hotwire anemometry is used to measure local velocity by placing a heated, fine wire into a flow stream and controlling the wire current that corresponds to the convective heat loss in the wire. Thus, hot wire anemometry has two components: a probe containing the heated wire and an anemometer which contains the necessary electronic components to control the wire current (i.e. wire temperature) and produce a conditioned measurement signal that is proportional to the velocity.

Hotwire anemometers are commonly made in two forms: a constant current type and a constant temperature type. Both types rely on the same physical

principle in that the energy generated within the wire is balanced by the convective heat loss from the flow. For equilibrium conditions, we can write an energy balance for the wire as:

Equation 3-1

$$I_w^2 R = hA_w(T_w - T_\infty)$$

In the constant current type, the heat generated in the wire, $I_w^2 R$, is held constant and the wire temperature, T_w, must be adjusted by the anemometer circuitry. In the constant temperature type, the wire current is adjusted to maintain a constant wire temperature.

Constant Temperature Anemometer

Constant temperature anemometers (CTA) were used in this research. A simplified schematic of an anemometer is shown in Figure 3-4 and the operation is based on a Wheatstone bridge where the $V_{A\text{-}B}$ voltage is balanced with $V_{C\text{-}D}$ with an operating current, I_{bridge}.

The decade resistance, R_3, is adjusted to set the bridge operating current that sets the operating wire current, I_w, and wire operating temperature. The other resistances, R_1 and R_2, are based on the resistance of the probe, probe support, cables, wire, and the bridge ratio of the anemometer.

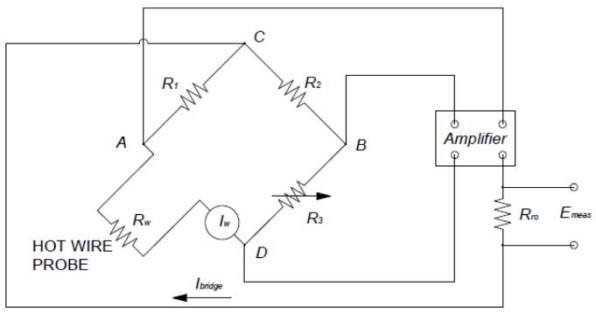

Fig. 3-4. Simplified hotwire anemometer circuit

As the resistance of the hot wire changes with velocity fluctuations, the bridge voltage is upset, and a feedback circuit (amplifier) adjusts the bridge current to maintain a constant wire temperature. A readout resistor senses the current changes and the wire voltage signal can be read from the DAQ or other measurement devices.

Hotwire probe

The Dantec Model 55P64 miniature wire probe, shown in Figure 3-5, was used for velocity measurement. It is a dual sensor, cross-wire (e.g. X-wire) type probe designed to measure Streamwise Velocity (U) and span-wise velocity (W) components. The probe wires are aligned such that they are in the same plane as the mean flow, as shown in Figure 3-6; however, the axis of the probe was perpendicular to the flow.

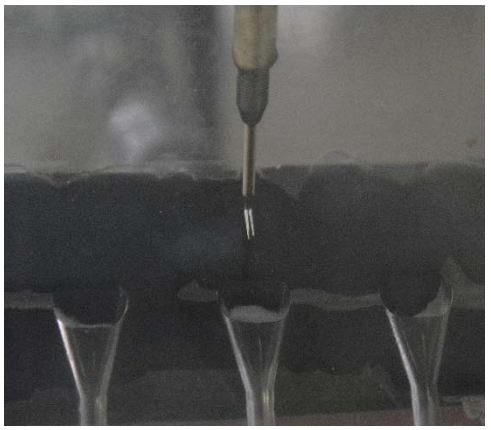

Fig. 3-5. Dantec Model 55p64 hot wire

Fig. 3-6.hot wire probe wire orientation

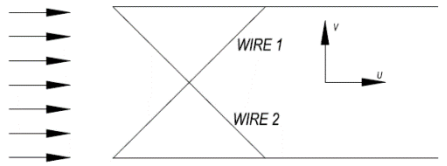

Hotwire Calibration

The Dantec Model 55P64 miniature wire probe was calibrated before performing the tests. As shown in figure 3-7, a small-scale wind tunnel was used for calibration. The air is blown into the calibration section, as the main flow, by an air compressor. Main flow total pressure and temperature, was obtained using a pressure transducer and a T-type thermocouple. Calibration

was made by changing the Yaw angles of the probe from -40° to +40° using a motor acquiring the pressure and two correspondent voltages values measuring by the probe. The calibrated velocity was calculated in terms of Mach number considering isentropic flow as follows:

$$Ma_{is} = \sqrt{\frac{2}{\gamma - 1}\left[\left(\frac{p_t}{p_0}\right)^{\frac{\gamma-1}{\gamma}} - 1\right]} \qquad \textit{Equation 3-2}$$

Where p_t is the total pressure, p_0 is the static pressure, while γ is specific heat ratio. Mainstream velocity could be calculated by equation 3-3:

$$V = \sqrt{\gamma RT}\, Ma_{is} \qquad \textit{Equation 3-3}$$

Where R is the gas constant, T is temperature.

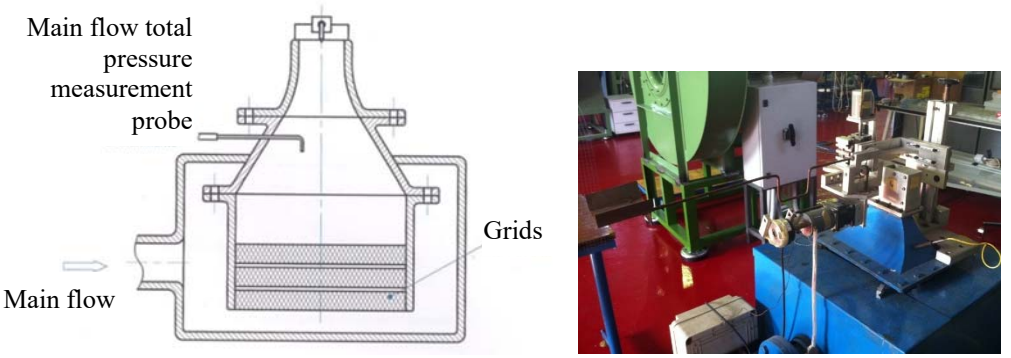

Fig. 3-7. Hotwire probe calibration system design and assembly.

Finally, the obtained calibration curve is shown in figure 3-8.

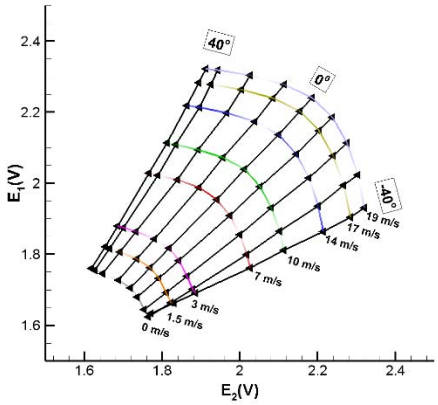

Fig. 3-8. Calibration curve for Dantec Model 55P64 miniature wire probe.

Hotwire Application

2-D flow field measurements have been carried out using Dantec Model 55P64 miniature wire probe at two locations downstream of coolant injection holes: at X=1D & X=5D (see fig. 3-9). A traverse system, as shown in figure 3-10, was used to cover measurement plane(Y, Z) including one mid-pitch to another one around the middle hole and vertically 3 diameters relative to the flat plate surface. Data acquisition is performed through a 12-bit resolution DAQ board, acquiring 20000 signals (20 kHz sampling frequency) at each location, assuring statistically accurate averages. The estimated uncertainty in the flow velocity and angle were respectively ± 3% of the reading and ±1deg.

3.4 Pressure Sensitive Paint Technique

PSP setup and data acquisition

FIB pressure sensitive paint was used in these experiments. According to the emission spectra of BinaryFIB paint, when the PSP paint is excited by a UV LED light at about 400 nm, two distinct signals are emitted: one at 560 nm and one at 650 nm. The former is the temperature signal, the latter is the

pressure/temperature signal. By taking the ratio of these signals it is possible to compensate the PSP sensitivity to temperature variation. The pressure sensitivity of BinaryFIB paint is about 0.6% per kPa, while the temperature sensitivity is 0.03% per °C [43].

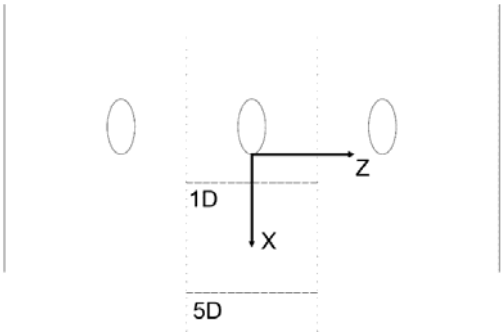

Fig. 3-9. Measurement location for HWA.

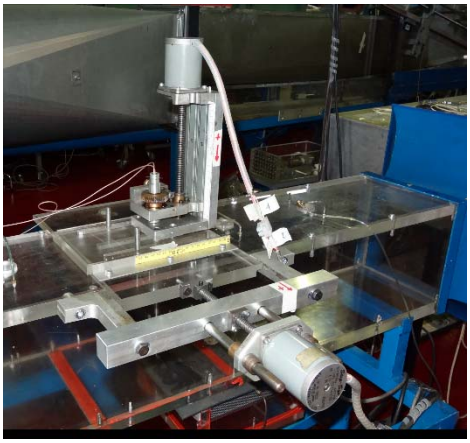

Fig. 3-10. Hotwire Anemometry Set-up.

As well known, PSP technique follows the Stern-Volmer law that states that the emission intensity is inversely related to the partial pressure of Oxygen [44]:

$$\frac{I_{ref}}{I} = A + B\,\frac{P}{P_{ref}} \qquad \textit{Equation 3-4}$$

Where, I_{ref} and I are emission intensity at reference (ambient) pressure P_{ref} and pressure P respectively, while A, and B are calibration coefficients. Where analogy between heat and mass transfer is valid, i.e. where the Lewis number is about one, it was shown [45, 46] that the adiabatic film cooling effectiveness can be written as:

$$\eta = 1 - \frac{C_{O_{2,fg}}}{C_{O_{2,air}}} \qquad \textit{Equation 3-5}$$

Where $C_{O_{2,fg}}$, and $C_{O_{2,air}}$ are the O_2 concentration field using a foreign gas (N_2) or (CO_2) and air as a coolant, respectively. When the molecular weight of foreign gas is similar to the air (N_2 case), equation (3-5) can be rewritten as:

$$\eta = 1 - \left(\frac{P_{O_{2,fg}}/P_{O_{2,wo}}}{P_{O_{2,air}}/P_{O_{2,wo}}}\right) \qquad \textit{Equation 3-6}$$

Otherwise:

$$\eta = 1 - \frac{1}{\left[1 + \left(\frac{P_{O_{2,air}}/P_{O_{2,ref}}}{P_{O_{2,fg}}/P_{O_{2,ref}}}\right)\frac{MW_{fg}}{MW_{air}}\right]} \qquad \textit{Equation 3-7}$$

Where $P_{O_{2,wo}}$ is the wind-off condition ;(i.e., a reference condition for which the exposed surface is at ambient pressure).The above pressure ratios must be obtained from the PSP calibration curve that in turn can be derived from eq. (3-4), considering that A, and B are a function of pressure and temperature. Calibration consists in recording with a CCD camera the light emitted by a PSP painted target surface properly illuminated for variable pressure at a constant

temperature. The same procedure could be repeated for different surface temperature.

In order to apply eq. (3-4) in practice, P/P_{ref} must be computed from different images. In fact, two different filters are used with binary PSP for detecting the temperature and pressure/temperature signals: a 550nm long pass filter for detecting the temperature dependent signal, and a 650nm long pass filter for detecting the pressure/temperature signal. Moreover, a further image is acquired in reference ambient condition with the UV lamp switched off (Dark image) and then subtracted to all the other images to compensate for any CCD camera defect. This gives a calibration curve that takes the following expression:

$$\frac{P}{P_{ref}} = a_2\left(\frac{R_{ref}}{R}\right)^2 + a_1\left(\frac{R_{ref}}{R}\right) + a_0 \qquad \textit{Equation 3-8}$$

Where R_{ref}/R is the ratio between the signals acquired through the two filters:

$$\frac{R_{ref}}{R} = \left(\frac{I_{ref} - I_{Dark}}{I - I_{Dark}}\right)_{650} \Big/ \left(\frac{I_{ref} - I_{Dark}}{I - I_{Dark}}\right)_{550} \qquad \textit{Equation 3-9}$$

PSP Calibration

In order to have a reliable result in PSP technique, efforts should be made to obtain a precise PSP calibration. Calibration was made by using a sealed chamber connected to a vacuum pump. The chamber was equipped with a pressure transducer, venting valve and it was designed to have an optical access over the test coupon. The test coupon is painted by PSP and it is installed over a heat exchanger in order to control its temperature. In fact, hot/cold water can be circulated through the heat exchanger to modify the test coupon temperature. T-type thermocouples are used to monitor the surface temperature and to

control the water inlet temperature that is adjusted to reach the desired value. Once the desired temperature is reached, the pressure inside the chamber is reduced down to about 1 kPa by using the vacuum pump. A set of 50 images of the test coupon is taken by the CCD camera (Flow Sense EO 4M, 2048pixel × 2048pixel resolution) with both red and green filters and then averaged to reduce the noise. By rapidly opening and closing the venting valve, the pressure inside the chamber is increased, resulting in a lower light intensity. This procedure is repeated until reaching the ambient pressure and then repeated for different temperature values. Figure 3-11(a) shows the calibration setup while Fig. 3-11(b) shows the calibration curves obtained in this study for variable temperature in the temperature range of 20°C-40°C. These curves almost coincide, demonstrating that binary PSP signal is not temperature dependent, at least over the investigated range. The calibration also allowed to quantify the uncertainty in the computed effectiveness value. Following the procedure described in [47] an uncertainty of $\delta\eta=\pm1.4\%$ with $\eta=0.5$ and of $\delta\eta=\pm15.6$ % when $\eta=0.1$ was computed.

(a) 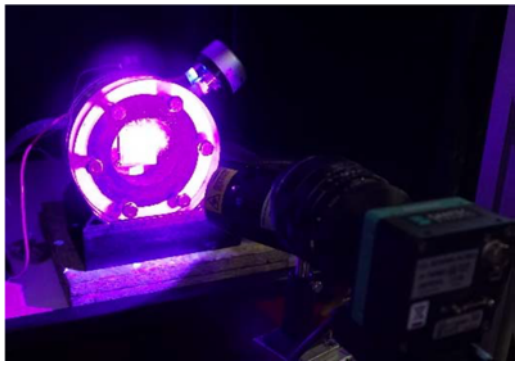 (b) 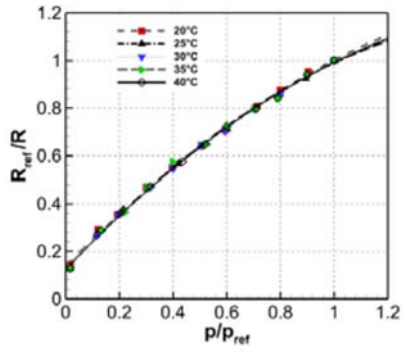

Fig. 3-11. (a) PSP calibration set up; (b) Calibration curves at variable temperature.

Once the PSP has been calibrated, the paint was applied on the flat plate surface (See fig. 3-12). The PSP was excited using a 400 nm LED light, and a CCD camera with a 2048 x 2048 resolution and a 12bit sensitivity with red and green filters, recorded the intensity emitted by the PSP one at a time (fig. 3-13). A multiple filter holder was designed and manufactured in order to fast changing the filter without moving the CCD camera. UV lamp and CCD camera were synchronized through the Timer Box of Dantec PIV system.

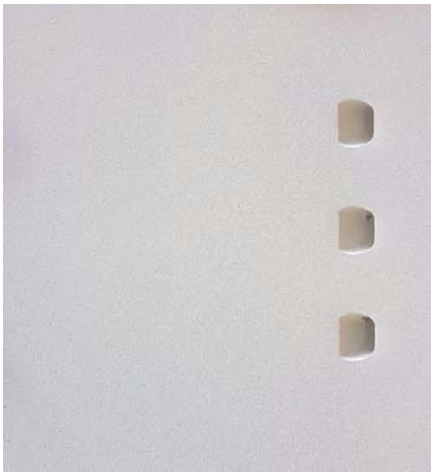

Fig. 3-12. Flat plate surface sprayed with PSP paint

For each blowing ratio, four set of images were required. The first set of images are the reference image, called wind-off; the PSP was excited with the UV lamp without any mainstream or coolant flow. The second set of images were the dark images in order to eliminate any noise in the images. The third set of images were the air images. These images were taken with mainstream and coolant flow, and the coolant through the film cooling holes was air. The fourth and final set of images were the Nitrogen or Carbon Dioxide images. Similar to the air image, these images were recorded with mainstream and

coolant flow, but the coolant flow was pure nitrogen N_2 or CO_2. In each case, 50 images were taken, then they were averaged to reduce the influence of noise.

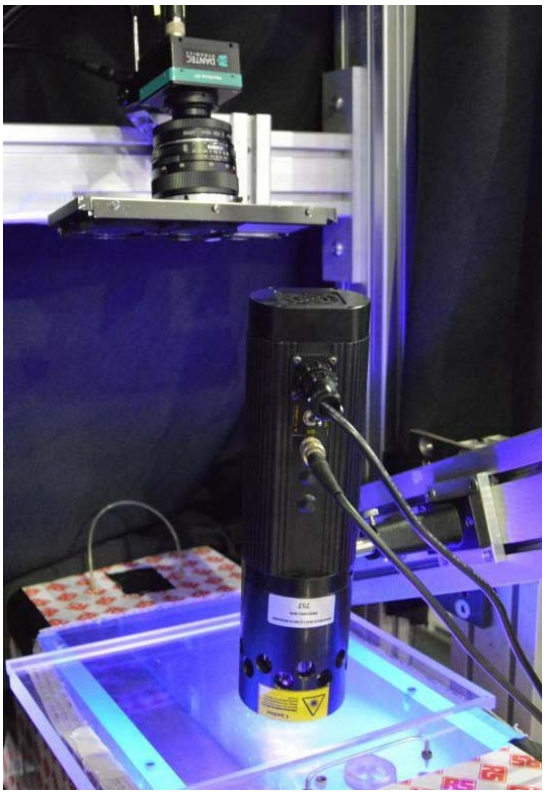

Fig. 3-13. PSP Experimental Set-up.

4

Set up and Instrumentation

The following chapter could be divided into two parts: the first part concerns the wind tunnel description while the second part describes the test conditions and summarizes the measurement planes.

4.1 Wind Tunnel

Tests were performed in the low-speed flat plate wind tunnel available at the Energy System and Turbomachinery Laboratory of the University of Bergamo. A photograph of the wind tunnel is shown in figure 4-1. A detailed description of wind tunnel and the design description is provided in the following.

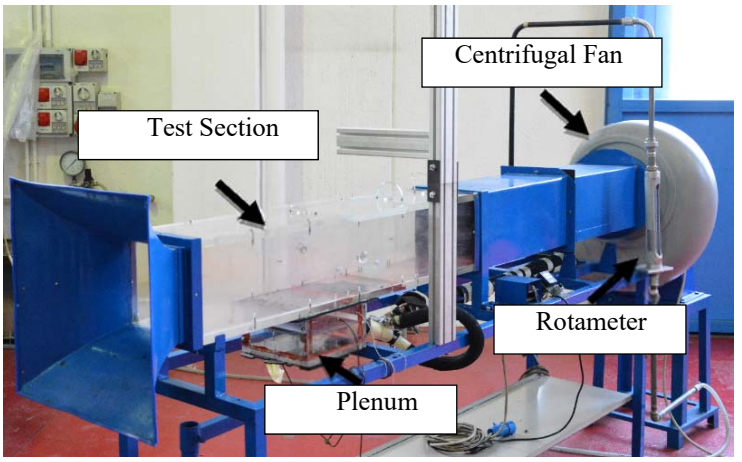

Figure 4-1. The wind tunnel at unibg.

The wind tunnel at Unibg is a continuous running suction type wind tunnel. The air is driven inside of the tunnel through an accelerating inlet section by means of a centrifugal fan. The tunnel cross section is 0.2 x 0.2 m^2, and it is 1.6 m long. The walls of the test section are optically transparent.

A secondary air supply system feeds the coolant to the holes through a plenum. Plenum, as shown in the Figure 4-2, is a box of 0.2×0.11 m with side inlet with a diameter of 15 mm which is located beneath the wind tunnel bottom wall.

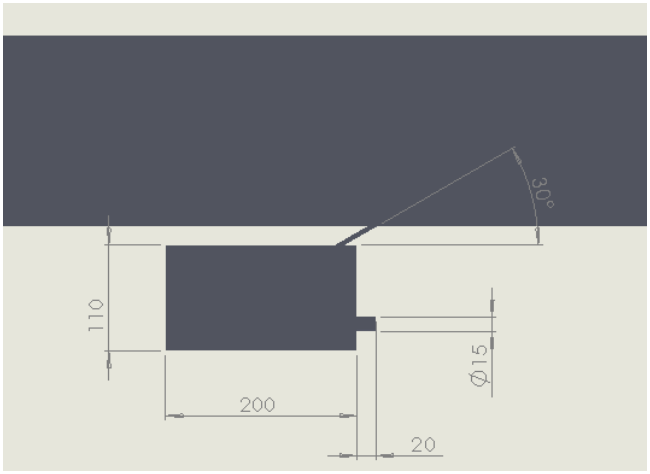

Figure 4-2. Schematic of the plenum.

In the present thesis work, two different hole configuration were investigated: Cylindrical hole and Fan-shaped hole (Fig. 4-3). In both configurations, a row of three 5 mm diameter holes is manufactured on the bottom wind tunnel wall. Holes are sharp edge without using any fillets which are inclined at 30° to the wall, their pitch-to-diameter ratio is P/D = 6 and their length to diameter ratio is L/D =8. The lateral expansion angle of the fan-shaped hole was 14°, resulting in a hole width of 13.98 mm at the hole exit. The chosen geometry of the fan-shaped hole is based on that of Gritsch et al. used in their research [11].

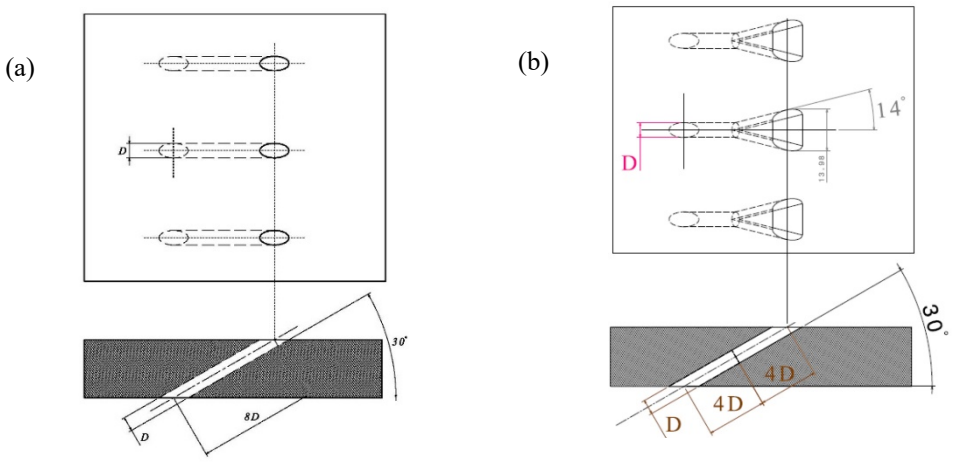

Figure 4-3. Schematic of flat plate (a) with cylindrical holes; (b) with fan-shaped holes.

4.2 Test conditions

Tests have been carried out at low speed, about 15 m/s, and low inlet turbulence intensity level, with blowing ratio ranging from 0.5 to 1.5 for cylindrical holes, and 1 from 2 for fan-shaped one. Pressure taps on the side wall (± 1 Pa) allow for a continuous monitoring of tunnel operating conditions. Coolant injection conditions are controlled measuring the injected flow rate and pressure (± 24 Pa) and the temperature inside the plenum. The injected flow rate is measured with a rotameter (± 2 l/min), while the temperature is measured with a T-type thermocouple (±0.5°C).

4.3 Measurement planes

Table 4-1 reports all planes that have been selected for different experimental measurements and their positions according to the reference coordinate system shown in figure 4-4.

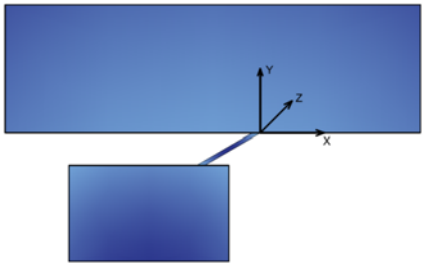

Figure 4-4. Reference coordinate position on test section.

It should be noted that origin of the reference coordinate system is located at the center of the middle hole (Z/D=0).

Table 4-1. Measurement plane positions.

Measurement Technique	**Plane**
PIV flow visualization	XY & XZ
PIV measurement	XY
Hotwire	YZ
PSP- TLC	XZ

5 COMPUTATIONAL SET UP

For this study, three different turbulence models, realizable k-ε (RKE), SST k-ω (SST KW), and Reynolds stress model (RSM), were tested and validated in the state-of-art CFD code STAR-CCM+ by simulating the wind tunnel flow with the two above-mentioned hole injection configurations (i.e. cylindrical and fan-shaped holes) at blowing ratio of BR=1. In this chapter, first of all, computational domain and boundary conditions that have been applied to these sets of CFD simulation are described in detail. Furthermore, a description of the three selected turbulence models will be given.

5.1 Computational Domains and Boundary Conditions

The computational domain in both cases, as shown in figure 5-1, includes the main test section, the jet hole, and the plenum. Main test section included inlet and outlet sections, tunnel walls. In the span-wise direction, the domain extends from one mid-pitch plane to another, containing a full injection hole. As mentioned by Foroutan et al. [48], it is important to include one full hole within the computational domain instead of considering the half hole with symmetric assumption at the hole centerline in order to accurately predicting lateral spreading of the jet.

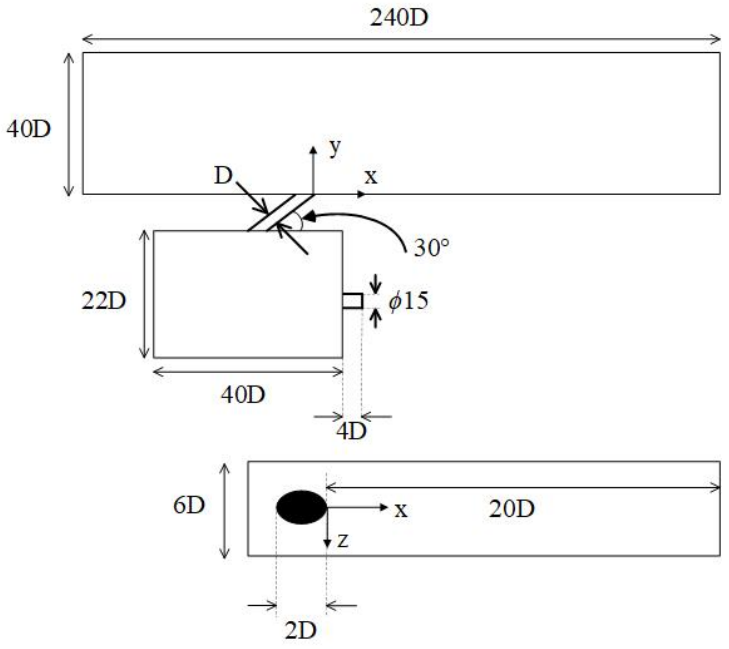

Figure 5-1. Schematic of computational domain.

A velocity inlet boundary condition was applied at the wind tunnel inlet with the velocity profile (fig. 6-2) and turbulence intensity profile measured by LDV technique. Besides, turbulent length scale, λ, was determined from following equation:

$$\lambda = 0.4\,\delta \qquad \textit{Equation 5-1}$$

In which δ is the boundary layer thickness calculated from the measured velocity profile. The turbulence length scale, λ, in equation (5-1) is a physical quantity that represents the size of the large eddies that contain energy in turbulent flows. A pressure outlet boundary condition, measured to be equal to atmospheric pressure, was applied at the outlet and smooth wall, no-slip boundary conditions were applied to the tunnel walls. A mass flow boundary

condition was applied at plenum inlet with coolant mass flow rate of 0.000957kg/s.

Moreover, values of turbulence intensity were determined from the following equation:

$$Tu_c = 0.16\, Re_c \qquad \textit{Equation 5-2}$$

This equation is derived from an empirical correlation for the core of a fully-developed duct flow. Coherently, the length scale for the coolant was computed by:

$$\lambda_c = 0.07\, D_{in} \qquad \textit{Equation 5-3}$$

where D_{in} is the diameter of hole inlet.

Initial condition for mainstream temperature set to 288°K as the ambient temperature during experiments, while the coolant temperature at plenum inlet was considered 323°K as it was measured during thermal measurements.

5.2 Grid generation

Meshing in Star CCM+ is mostly automated and based on the meshing model selected and cell size, cell growth, and refinement settings. In the present study, the polyhedral mesh model was chosen because it's relatively easy and efficient to build, requiring no more surface preparation than the equivalent tetrahedral mesh. It also contains approximately five times fewer cells than a tetrahedral mesh for a given starting surface [49].

A close-up of the midplane view of the grid in the near-field region is depicted in Figure 5-2. The base mesh size was initially set to 0.03 m and refinement through the domain was controlled by growth parameters. The grid

is refined in areas of large gradients. Also, eight layers of prismatic cells were added near the wall as shown in figure 5-3. Since turbulence models utilized in this study are used with a two-layer zonal model for near-wall treatments, it is important that the y^+ values of the grid point closest to the wall be of the order of unity.

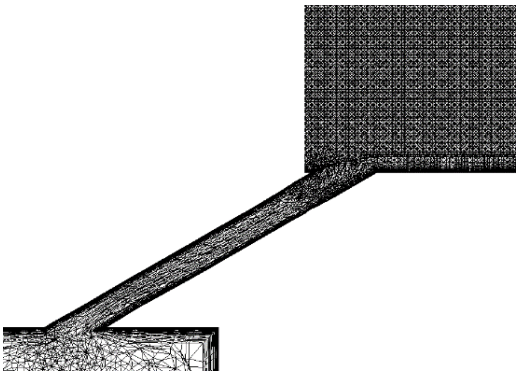

Figure 5-2. Close-up of the midplane view of the grid near the injection region.

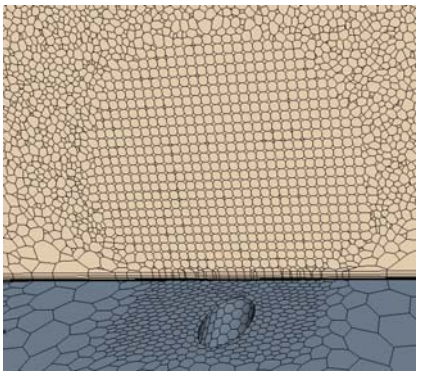

Figure 5-3. Prism layer meshes near wall

Moreover, a part-based meshing scheme was employed since it allows the mesh refinement using a volumetric control such as sphere or block within a specific volume. For example, for both injection hole configurations, a cylindrical volumetric control was used to refine the mesh near the desired hole. Figure 5-4 depicts mesh refinement for middle hole using a cylindrical volumetric control for cylindrical and fan-shaped configurations.

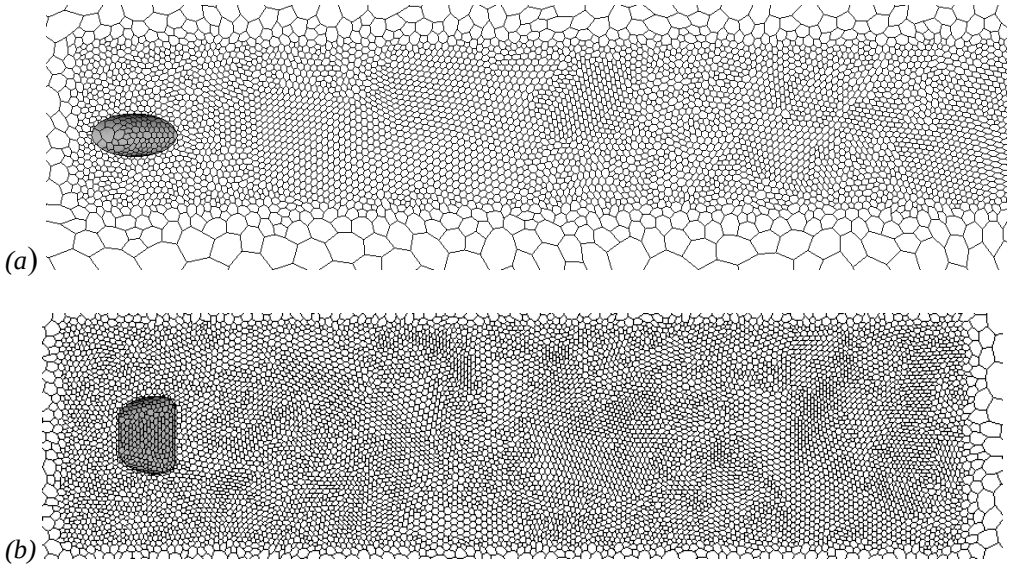

Figure 5-4. Mesh refinement near wall, (a) cylindrical hole; (b) fan-shaped hole.

Three grid were investigated for sensitivity analysis (See 6.1.2.1 & 6.2.2.1).

5.3 Governing equation

The present study investigates the flow field and thermal characteristics in the near-field region of film cooling jets through numerical simulations using Reynolds-averaged Navier– Stokes (RANS) models. The working fluid is assumed to be incompressible and Newtonian with temperature-dependent fluid properties. The governing transport equations are the continuity, momentum, and energy equations as following:

- Continuity Equation:

$$\frac{\partial U_i}{\partial x_i} = 0 \qquad \textit{Equation 5-4}$$

- Momentum Equations:

$$U_j \frac{\partial U_i}{\partial x_j} = -\frac{1}{\rho}\frac{\partial P}{\partial x_i} + \frac{\partial}{\partial x_j}\left(\vartheta \frac{\partial U_i}{\partial x_j} - \overline{\acute{u}_\iota \acute{u}_J}\right) \qquad \textit{Equation 5-5}$$

- Energy Equation:

$$U_j \frac{\partial T}{\partial x_j} = \frac{\partial}{\partial x_j}\left(\alpha \frac{\partial T}{\partial x_j} - \overline{\acute{u}_j \acute{T}}\right) \qquad \textit{Equation 5-6}$$

In these equation Reynolds stresses ($\overline{\acute{u}_\iota \acute{u}_J}$) and turbulent heat transfer $\overline{\acute{u}_J \acute{T}}$ have to be modeled using the following equations:

$$\overline{\acute{u}_\iota \acute{u}_J} = -\frac{\mu_t}{\rho}\left(\frac{\partial U_i}{\partial x_j} + \frac{\partial U_j}{\partial x_i}\right) + \frac{2}{3} k \delta_{ij} \qquad \textit{Equation 5-7}$$

$$\overline{\acute{u}_J \acute{T}} = -\frac{\mu_t}{\rho \sigma_k} \frac{\partial T}{\partial x_j} \qquad \textit{Equation 5-8}$$

For the steady RANS simulations, the SST k-ω turbulence model, the Realizable k-ε turbulence model, and Reynolds stress model provided closure. SST k-ω, and Realizable k-ε were used in the present work since they are the most widely used and well-known two-equation turbulence models that often provide reasonable prediction in a relatively short computer run time. However, these two turbulence models fail to resolve the highly complex flow-field near the film cooling hole created by the jet-mainstream interaction. RSM model is more advanced turbulence model which takes into account anisotropy in the wake and provide a better prediction of the stress field.

In the following, more emphasis will be given to the turbulence models used in this study.

5.3.1 Realizable k-ε model

K-Epsilon turbulence model has been widely used in an industrial application for several decades. The Realizable Two-Layer K-Epsilon model is selected for this project. The two-layer approach enables it to be used with fine meshes that resolve the viscous sublayer. Considering the k-ε model, two differential equations must be solved: one for the turbulent kinetic energy and the other for the dissipation rate [49]:

$K\ equation$:

$$\rho\, U_j \frac{\partial k}{\partial x_j} = \frac{\partial}{\partial x_j}\left[\left(\mu + \frac{\mu_t}{\sigma_k}\right)\frac{\partial k}{\partial x_j}\right] + \mu_t\left(\frac{\partial U_i}{\partial x_j} + \frac{\partial U_j}{\partial x_i}\right)\frac{\partial U_i}{\partial x_j} - \rho\varepsilon \qquad \textit{Equation 5-9}$$

$\varepsilon\ equation$:

$$\rho\, U_j \frac{\partial \varepsilon}{\partial x_j} = \frac{\partial}{\partial x_j}\left[\left(\mu + \frac{\mu_t}{\sigma_\varepsilon}\right)\frac{\partial \varepsilon}{\partial x_j}\right] + C_{\varepsilon 1}\mu_t \frac{\varepsilon}{k}\left(\frac{\partial U_i}{\partial x_j} + \frac{\partial U_j}{\partial x_i}\right)\frac{\partial U_i}{\partial x_j} - \rho C_{\varepsilon 2}\frac{\varepsilon^2}{k} \qquad \textit{Equation 5-10}$$

Where $\mu_t = C_\mu \rho \frac{k^2}{\varepsilon}$ and $C_\mu = 0.09, C_{\varepsilon 1} = 1.44, C_{\varepsilon 2} = 1.92, \sigma_k = 1.0$ and $\sigma_\varepsilon = 1.3$.

These constant were adopted according to recommendations of Launder et al. [50].

5.3.2 SST k-ω model

A K-ω model is a two-equation model and it is an alternative to the K-ε. The transport equations that are solved are for the turbulent kinetic energy, *k*, and a

quantity called ω, which is defined as the specific dissipation rate, that is, the dissipation rate per unit turbulent kinetic energy. One advantage of K-ω model is its improved performance for boundary layers under adverse pressure gradients. The boundary layer computation is very sensitive to the values of turbulent kinetic energy quantity in the free stream in the original form of K-ω model. In this thesis, we used SST (shear-stress transport) K-omega model which effectively blends a K-ε model in the far-field with a K-ω model near the wall. The low-y+ wall treatment is selected.

Equation 5-11

$K\ equation$:

$$\frac{Dk}{Dt} = \frac{P}{\rho} - \beta^* \omega k + \frac{1}{\rho}\frac{\partial}{\partial x_j}\left[(\mu + \sigma_k \mu_t)\frac{\partial k}{\partial x_j}\right] - \frac{\partial(u_j k)}{\partial x_j}$$

$\omega\ equation$:

$$\frac{D\omega}{Dt} = \frac{\gamma}{\vartheta_t}\frac{P}{\rho} - \beta\omega^2 + \frac{1}{\rho}\frac{\partial}{\partial x_j}\left[(\mu + \sigma_\omega \mu_t)\frac{\partial \omega}{\partial x_j}\right] + 2[1 - F_1]\frac{\sigma_{\omega 2}}{\omega}\frac{\partial k}{\partial x_j}\frac{\partial \omega}{\partial x_j} - \frac{\partial(u_j \omega)}{\partial x_j}$$

Equation 5-12

Constants value and exact definition of each parameter in equation 5-12 were described in detail in the work of Menter et al. [51].

5.3.3 Reynolds Stress Transport (RSM) Turbulence model

Reynolds Stress Turbulence models are the most complex turbulence models in STAR-CCM+ [49] which solve six equations for the Reynolds stress components besides one equation for the turbulent dissipation, ε. It accounts for anisotropy effects due to strong swirling motion, streamlines curvature. The Quadratic Pressure Strain RSM is chosen in this study with considering high-y+ wall treatment.

Considering RSM turbulence model, closure for the Reynolds stress tensor in steady RANS simulation is obtained by solving time-averaged transport equation for the Reynolds stresses as following:

$$U_k \left. \overline{\partial \acute{u}_i \acute{u}_j} \right/ \partial x_k = P_{ij} + D_{ij}^{\vartheta} + D_{ij}^{T} + \varphi_{ij} - \varepsilon_{ij} \qquad \textit{Equation 5-13}$$

The production, Pij, and viscous diffusion, D_{ij}^{ϑ} require no additional modeling effort while the turbulent diffusion,D_{ij}^{T} the pressure strain correlation, φ_{ij} and the dissipation rate, ε_{ij} require a model for their closure.

Turbulent diffusion is modeled with the isotropic formulation from Lien and Leschziner [52] as:

$$D_{ij}^{T} = \frac{\partial}{\partial x_k}\left(\left(\vartheta + \frac{\mu_t}{\sigma_k}\right) \left. \overline{\partial \acute{u}_i \acute{u}_j} \right/ \partial x_k\right) \qquad \textit{Equation 5-14}$$

where the Prandtl number for the turbulence kinetic energy is σ_k=0.82 and the turbulent viscosity is computed from equation (5-15).

$$\mu_t = C_\mu \rho \frac{k^2}{\varepsilon} \qquad \textit{Equation 5-15}$$

The turbulent dissipation tensor, ε_{ij} is modeled by assuming isotropy of the small dissipative eddies as shown in equation 5-16.

$$\varepsilon_{ij} = \frac{2}{3}\varepsilon\delta_{ij} \qquad \textit{Equation 5-16}$$

with the transport equation for the turbulent dissipation rate, ε computed from equation 5-17.

$$\frac{D\varepsilon}{Dt} = \frac{1}{\rho}\frac{\partial}{\partial x_j}\left(\left(\mu + \frac{\mu_t}{\sigma_\varepsilon}\right)\frac{\partial \varepsilon}{\partial x_j} + C_{\varepsilon 1}\frac{\varepsilon}{k}\frac{1}{2}P_{ii} - C_{\varepsilon 2}\frac{\varepsilon^2}{k}\right) \qquad \textit{Equation 5-17}$$

The pressure-strain correlation term,φ_{ij} is modeled based on the quadratic formulation of Speziale, Sarkar, and Gatski [53]. This model is written as follows:

$$\varphi_{ij} = -(C_1\rho\varepsilon + C_1^* P)b_{ij} + C_2\rho\varepsilon\left(b_{ik}b_{kj} - \tfrac{1}{3}b_{mn}b_{mn}\delta_{ij}\right) + \left(C_3 - C_3^*\sqrt{b_{ij}b_{ij}}\right)\rho k + C_4\rho k\left(b_{ik}S_{jk} + b_{jk}S_{ik} - \tfrac{2}{3}b_{mm}S_{mm}\delta_{ij}\right) + C_5\rho k\left(b_{ik}\Omega_{jk} + b_{jk}\Omega_{ik}\right) \qquad \textit{Equation 5-18}$$

where b_{ij} is the Reynolds-stress anisotropy tensor defined as:

$$b_{ij} = -\left(\frac{-\rho\overline{\acute{u}_\iota \acute{u}_J} + \frac{2}{3}\rho k\delta_{ij}}{2\rho k}\right) \qquad \textit{Equation 5-19}$$

The mean strain rate, S_{ij}, is defined as:

$$S_{ij} = \frac{1}{2}\left(\frac{\partial u_j}{\partial x_i} + \frac{\partial u_i}{\partial x_j}\right) \qquad \textit{Equation 5-20}$$

The mean rate-of-rotation tensor, Ω_{ij} is defined by:

Equation 5-21

$$\Omega_{ij} = \frac{1}{2}\left(\frac{\partial u_i}{\partial x_j} + \frac{\partial u_j}{\partial x_i}\right)$$

Values for the constants and coefficients used for the quadratic pressure-strain RSM equations are listed in Table 5-1.

Table 5-1. Coefficients for the quadratic pressure-strain model.

C_1	C_1^*	C_2	C_3	C_3^*	C_4	C_5
3.4	1.8	4.2	0.8	1.3	1.25	0.4

5.4 Computational Method

Three-dimensional steady incompressible flow simulation was performed on the flat plate wind tunnel. Air considered as an ideal gas. The segregated solver of Star CCM+ was used which solves the flow equations (one for each velocity component and one for pressure) in a second-order, uncouple manner. Moreover, The Segregated Fluid Temperature model solves the total energy equation with temperature as the solved variable [49].

For all simulations, values of the residuals, velocity, and temperature were monitored for convergence. Simulations were considered to be converged when velocity at one diameter downstream of middle hole and temperature on the flat plate surface did not change more than 0.01% for at least 100 iterations. Besides, the relative residuals for all parameters dropped by at least five orders of magnitude when the solution had converged in all simulations.

6 RESULTS

This chapter is divided into three parts: first part presents experimental result for the cylindrical hole configuration for BR=0.5-1.5. Then, steady RANS simulations were performed assessing three turbulence models for BR=1 in order to select the best turbulence model for prediction of film cooling jet behavior for the cylindrical hole. The second part includes experimental and numerical results for the fan-shaped hole configuration, respectively, for BR=1-2, and BR=1. The third part concerns density ratio effect for BR=1 in case of a cylindrical hole.

6.1 Cylindrical hole

This section presents the experimental results of the cylindrical hole for BR=0.5-1.5 as well as the numerical results for BR=1.

6.1.1 Experimental Results

Experimental results include cylindrical hole characterization, aerodynamic and thermal investigation of jet and mainstream interaction.

6.1.1.1 Discharge Coefficient

Injection condition for cylindrical holes was characterized through the measurement of discharge coefficient. The discharge coefficient C_d is the ratio of actual mass flow rate to the ideal mass flow rate through the film-cooling

hole. The ideal mass flow rate is calculated assuming an isentropic one-dimensional expansion from the total pressure in the plenum $p_{t,c}$ to the static pressure in the free stream p_e [54].This leads to:

$$C_d = \frac{\dot{m}}{p_{t,c}\left(\frac{p_e}{p_{t,c}}\right)^{\frac{\gamma+1}{2\gamma}}\sqrt{\frac{2\gamma}{\gamma-1}RT_{t,c}\left(\left(\frac{p_{t,c}}{p_e}\right)^{\frac{\gamma-1}{\gamma}}-1\right)}\,\pi\frac{D^2}{4}}$$

Equation 6-1

The coolant total pressure was measured by pressure taps on the side-wall of the plenum. The static pressure of free stream was measured by pressure tap at the top wall of the tunnel. Figure 6-1 shows the C_d distribution versus the ratio of coolant pressure $p_{t,c}$ to the free stream static pressure p_e, The discharge coefficient shows the typical behavior of cylindrical holes, reaching an almost constant value of about 0.65 for pressure ratios greater than 1.004.

6.1.1.2 Aerodynamic Survey

Flow Characteristic of the oncoming boundary Layer

The characteristic of the oncoming boundary layer of mainstream flow was measured by using LDV system 7D upstream the injection hole trailing edge. Figure 6-2 shows the boundary layer profile as well as turbulence intensity profile. From the measurement results given in Figure 6-2, it can be seen clearly that, the velocity profile in the boundary layer of the oncoming mainstream flow was found to follow a1/7 power law well. The boundary layer thickness is 1.24D, while its displacement thickness and shape factor are 0.142D and 1.37 respectively, indicating a fully turbulent boundary layer. A free stream turbulence intensity of about 0.6% was also detected.

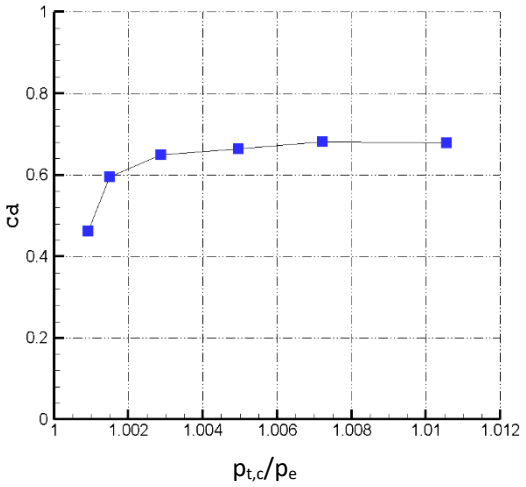

Figure 6-1. hole discharge coefficient.

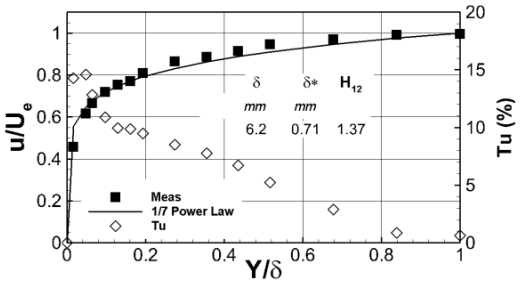

Figure 6-2. Oncoming boundary layer.

Boundary layer profile downstream of the holes at hole centerline

Results from LDV measurements at hole centerline are reported in Figure 6-3 and Figure 6-4 in terms of profiles of time-averaged streamwise velocity component and streamwise and wall normal rms velocities at X/D = 1 and X/D = 5, respectively. Data are normalized with respect to the mainstream velocity U_e.

For blowing ratio less than 1, the velocity profile in Figure 6-3a shows that the film cooling jet stays close to the flat plate surface with velocity always lower than the free stream one. These low velocities, associated with low fluctuations (Fig. 6-3b-c) indicate a moderate mixing between the coolant and

mainstream flows. On the other hand, when the blowing ratio becomes greater than 1, the stream-wise velocity profile is characterized by a profound peak that becomes even higher than $1.5U_e$ for the maximum BR = 1.5. The elevation of this peak climbs by increasing the blowing ratio. Figures 6-3b, c depict high-velocity fluctuations, especially at the jet to mainstream interfaces, and a certain degree of anisotropy, especially for the maximum BR = 1.5. These three figures indicate a strong mixing between the coolant and main flow with a consequent fast jet spreading in the wall-normal direction.

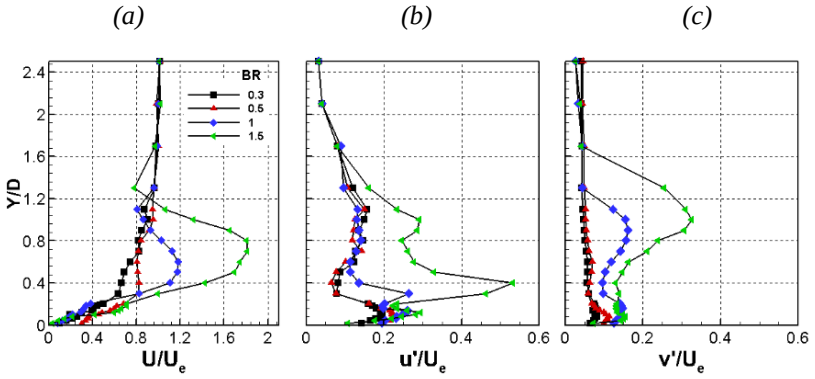

Figure 6-3. Boundary layer Profiles at X/D=1.

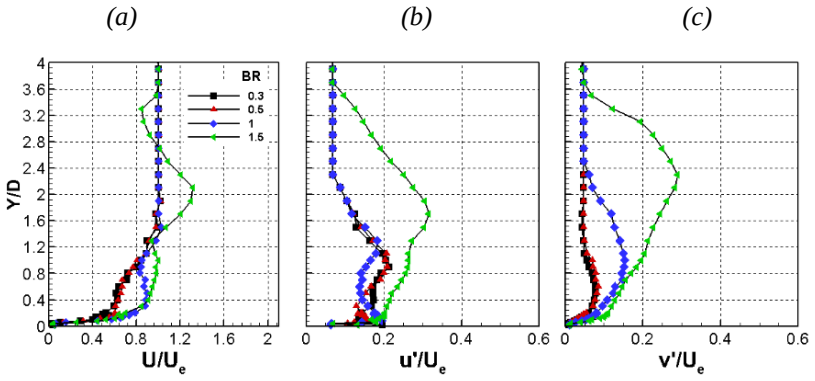

Figure 6-4. Boundary layer profiles at X/D=5.

Comparing Figure 6-3a and Figure 6-4a shows that the streamwise velocity peak value decreases as the coolant travels along the flat plate surface from 1 to 5 diameters downstream of the hole due to the mixing with the mainstream. As a result, the jet is spreading over a larger area. Large values for both fluctuating velocity components can still be observed 5D downstream of injection location, but at a higher elevation from the wall and with a more uniform distribution across the jet.

2D flow field in (X, Y) plane at Z/D=0

PIV technique was used to characterize the mean and turbulent flow distribution over a 2-D plane located at mid hole centerline (Z/D=0). Normalized mean velocity flow fields in the near-hole region for blowing ratio of 0.5, 1 and 1.5 are shown in figures 6-5. As clearly shown in the Figure 6-5a for blowing ratio less than 1, the coolant jet stays attached to the surface of the flat plate, thereby forming a film over the test plate downstream of the holes. For the cases with BR greater than 1, (Fig. 6-5b, c), coolant jet lifts off the flat plate surface. Also, a remarkable over speed is observed in the center of the jet for BR=1.5, which is in agreement with LDV result.

In addition, figure 6-6 show the Turbulence level contours in the streamwise plane for the aforementioned blowing ratio. The peak turbulence level for BR0.5 to 1.5 are 11%, 22%, and 26%, respectively. The peak turbulence for the BR less than and equal to 1 happens at X/D=1 as shown in Figure 6-6 (a-b) while for high blowing ratio (BR=1.5) it locates at hole exit which indicates separation inside the holes.

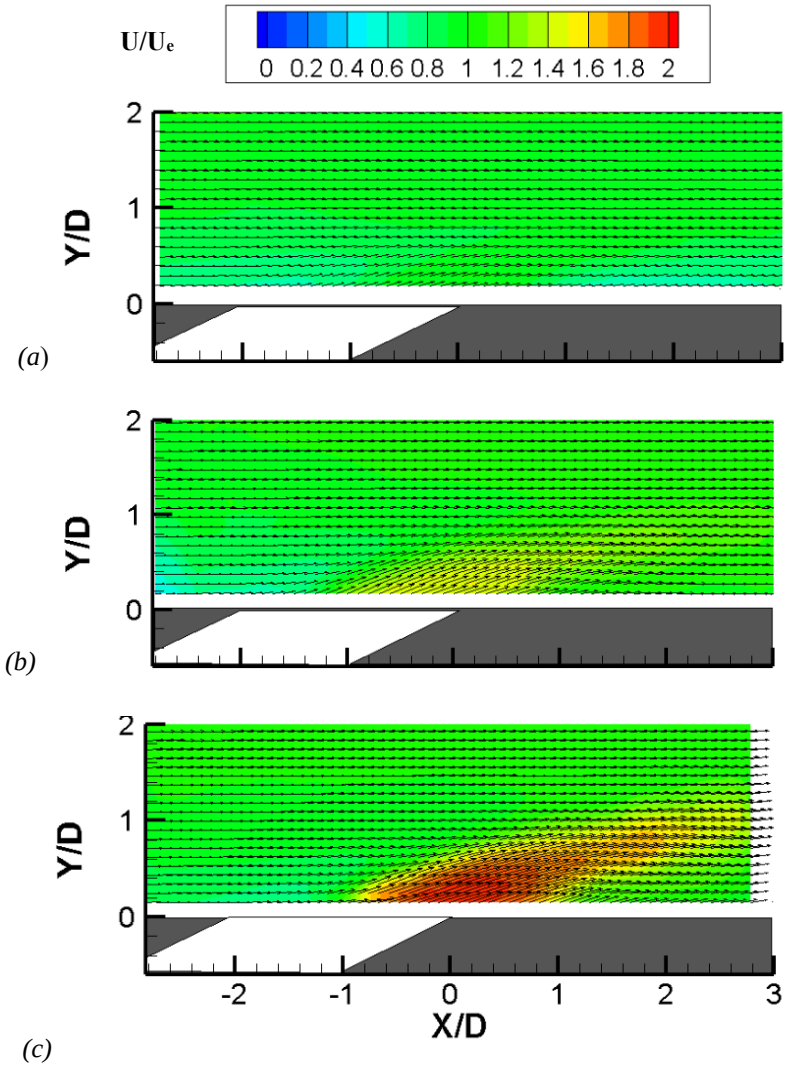

Figure 6-5. Flow velocity fields at Z/D = 0: (a) BR = 0. 5; (b) BR = 1; (c) BR = 1.5.

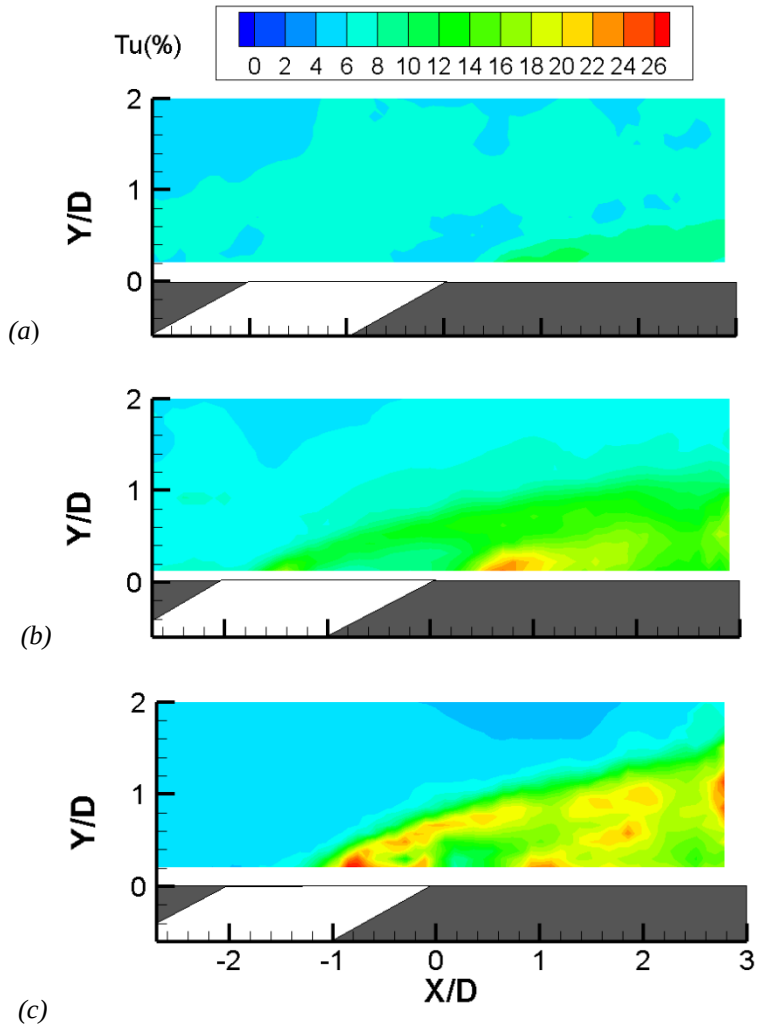

Figure 6-6. Turbulence level contours at Z/D = 0: (a) BR = 0. 5; (b) BR = 1; (c) BR = 1.5.

Flow Visualization

To investigate the unsteady behavior of coolant to mainstream mixing process, flow visualization performed over two planes: (X, Y) and (X, Z) planes. Figure 6-7 reports flow visualizations for variable injection conditions. In particular, Fig. 6-7a shows the coolant jet at the lowest blowing ratio of BR = 0.5. Along the centerline of the jet (Z/D = 0), the coolant flow remains attached to the surface downstream of the film cooling hole. 9 diameters

downstream of the film cooling hole, the vertical spread of the jet is limited to 1 diameter in the vertical direction (Y/D = 1). Counter-clockwise vortical structures due to the breakdown of the Kelvin Helmholtz instability of the shear layers already appears at this low injection condition relatively far from the hole. This injection condition is higher than the one at which hairpin vortices were observed on a film cooled vane [35], but it is similar to the one at which counter-clockwise vortices were observed.

By increasing the blowing ratio to 0.75 (Fig. 6-7b), these structures appears closer to injection location and result to be defined better. Film cooling jet is still attached to the flat plate surface but the vertical spread of the jet is higher than at BR = 0.5. Figures 6-7c, d demonstrate cases in which blowing ratio is larger than 1. Cooling jet begins to lift off the surface. For blowing ratio 1.5, the vertical spread of the jet has a height of 6D with respect to the flat plate surface which give rise to the loss of thermal protection on the flat plate surface. Moreover, counter-clockwise vortical structures dominate the jet behavior which are always highly unsteady.

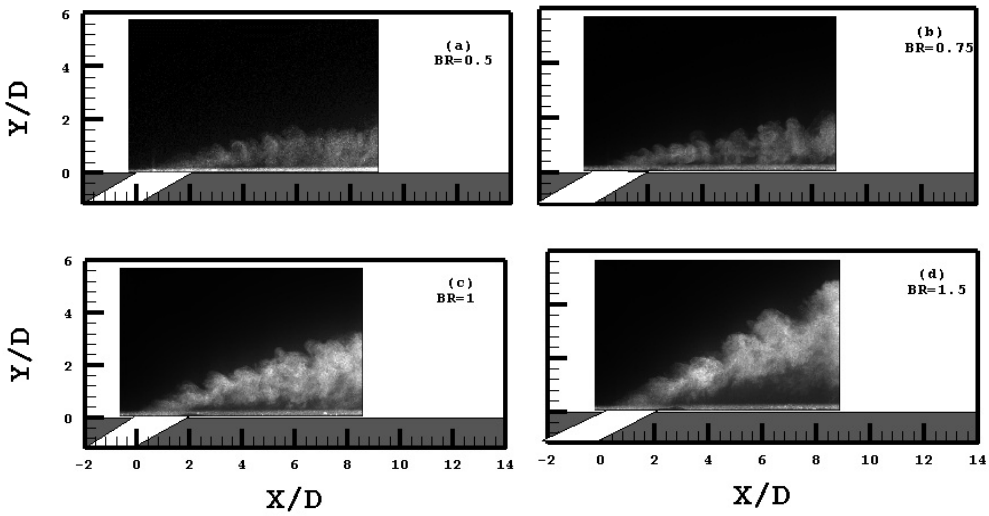

Figure 6-7. Flow Visualization of film cooling jet: (a) BR = 0.5; (b) BR = 0.75, (c) BR = 1.0, (d) BR = 1.5

Finally, figures 6-8a,b show flow visualization of film cooling jet on the flat plate surface capturing the behavior of the cooling jet leaving three holes for BR = 1 and 1.5. It was not possible to capture images for blowing ratio less than 1, since the cooling film jet is attached to the surface and jet spreading in the wall-normal direction is not large enough to allow a clear jet detection. Comparison of Figure 6-8a with Figure 6-8b makes it clear that by increasing the blowing ratio jets spread over a larger area even in the lateral direction. Nevertheless, jets do not merge in the investigated domain. The coherent structures can also be observed from this point of view.

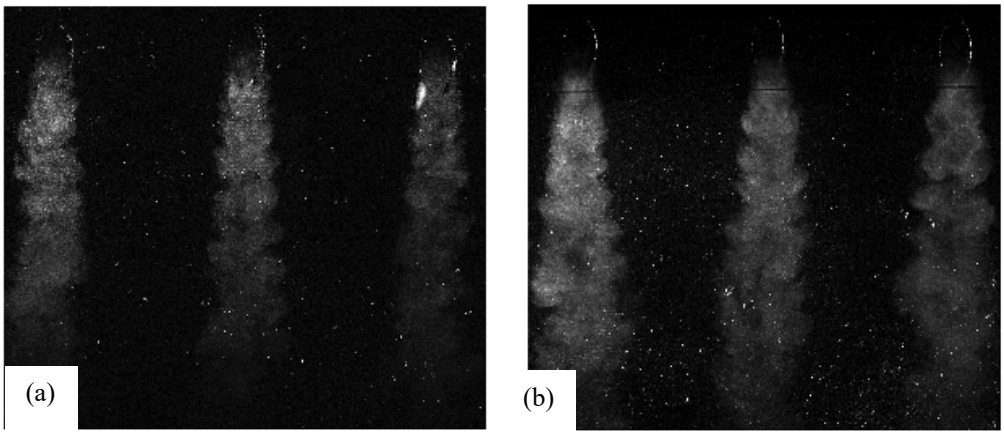

Figure 6-8. Flow Visualization of film cooling jet on flat plate surface: (a) BR = 1.0; (b) BR = 1.5.

2-D flow field in (Y, Z) plane

Hotwire anemometry was used to characterize the coolant to mainstream interaction in (Y, Z) plane at X=1D, X=5D.

❖ Near Field of Jet-Crossflow Interaction

Figure 6-9 shows the streamwise velocity in a vertical-lateral plane for BR=1, 1.5 at 1 diameter downstream of the injection hole. As it is clear in these figures, lateral spreading of film cooling jet at BR=1.5 is wider than BR=1, and velocity peak happens at higher elevation. In both cases, cooling jet lift off from

the flat plate surface. The peak turbulence levels for the BR=1, and BR=1.5 are Tu = 21, and 26%, respectively. These values for turbulence intensity is in agreement with that of measured with PIV technique.

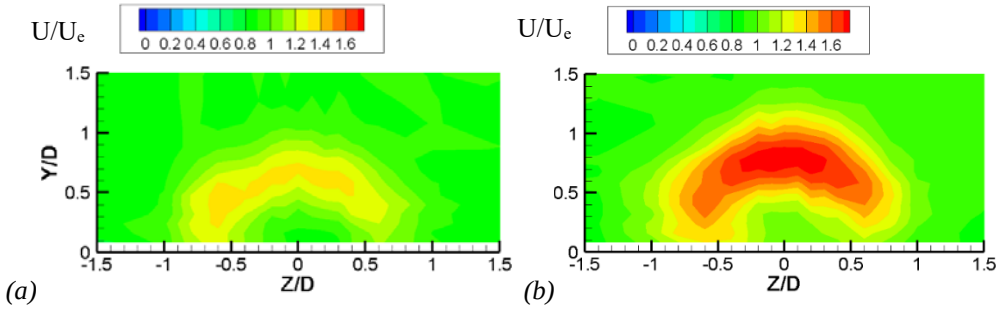

Figure 6-9. Normalized streamwise velocity contours at X=1D: (a) BR = 1.0; (b) BR = 1.5.

❖ Downstream of Jet-Crossflow Interaction

Figures 6-10 shows the streamwise velocity in the same plane for BR=1, 1.5 at 5 diameter downstream of the injection hole. At this location, the secondary flow becomes negligible and jet shows wake-like structure which indicates diffusion of the coolant as it travels downstream of injection holes. At this location, far from injection holes, peak turbulence level decreases to 14% for both blowing ratios.

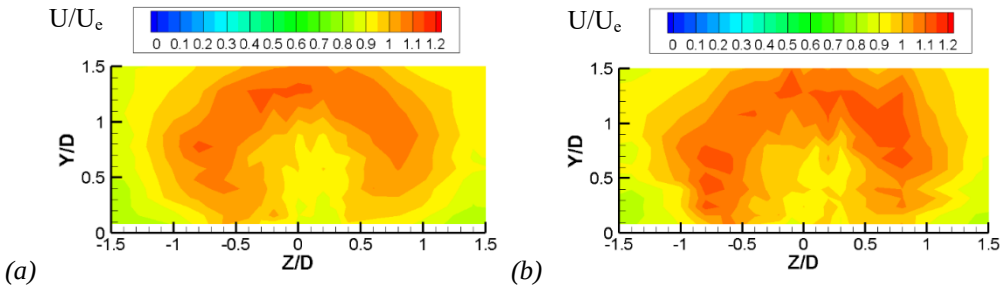

Figure 6-10. Normalized streamwise velocity contours at X=5D: (a) BR = 1.0; (b) BR = 1.5.

Comparison LDV- PIV- HW Results

Figures 6-11 show normalized streamwise velocity for BR=1 obtained from LDV, PIV, and HW measurement techniques at X=1D. As shown in figure 6-11, streamwise velocity obtained from LDV, PIV, and HW measurements are in agreement, although the jet core peak measured from LDV measurements are less than two other measurements. This difference in peak values could be due to the fact that during LDV measurement laser beams weren't exactly in the center of middle hole.

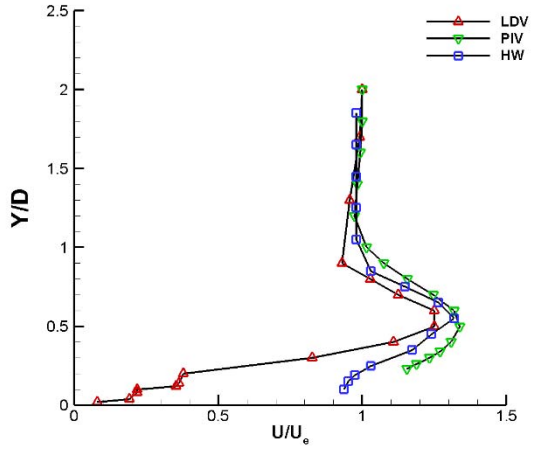

Figure 6-11. Normalized streamwise velocity profiles at X=1D for BR=1 obtained from LDV, PIV, and HW measurements.

6.1.1.3 Thermal Results

PSP technique was used to measure adiabatic film cooling effectiveness on the surface of the flat plate. Figure 6-12 (a) gives the film cooling effectiveness distribution downstream of the cylindrical injection hole in the middle of the flat plate at the blowing ratio of BR=0.5 measured by PSP technique. The TLC

measurement result in the same condition was also given in figure 6-12(b) for the back-to back comparison. It can be clearly seen that film cooling effectiveness distribution obtained by PSP techniques agrees well in general with the TLC. However, some minor differences can be identified based on comparison of Figure 6-12(a), and 6-12(b). For example, for the region near peak cooling effectiveness from 3<x/D<10, the PSP measurement results seem to be slightly lower than the TLC results. Such discrepancy is due to the effect of heat conduction over the flat plate, particularly in the lateral direction.

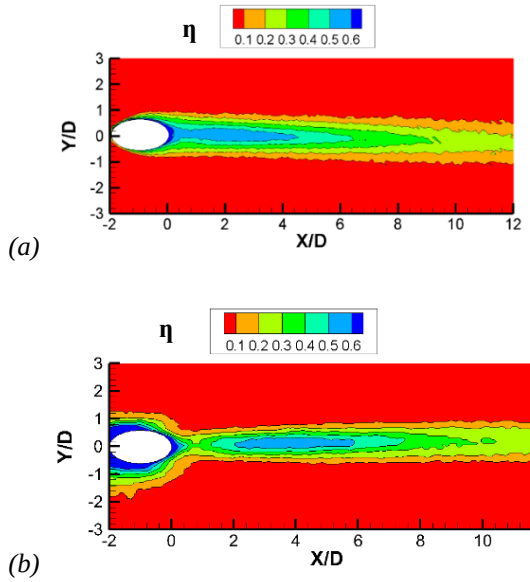

Figure 6-12. Comparison of the cooling effectiveness distribution for BR=0.5: (a) PSP; (b) TLC.

Figure 6-13 shows the laterally-averaged cooling effectiveness profile of the present study as a function of the downstream distance from the exit of the injection hole at the blowing ratio of BR=0.5 and BR=1. Some published data in literature with the very comparable coolant hole configuration and test condition as those of present study are also given in the plot for a quantitative comparison. PSP results of the present investigation are in good agreement with the literature for both the tested injection cases.

Figure 6-14 shows adiabatic film cooling effectiveness contour at different blowing ratio of BR=0.5, 1, and 1.5, for cases with Nitrogen as coolant stream. Furthermore, figure 6-15 and figure 6-16 shows the profiles of the measured cooling effectiveness along the centerline of the coolant injection hole and the laterally-averaged film cooling effectiveness as a function of the distance away from the coolant injection hole respectively. It can be clearly seen that, for blowing ratio less than 1 (i.e. BR=0.5), the cooling jet remains attached to the surface which leads to increased film cooling effectiveness downstream of the film cooling hole. Downstream as the cooling jet spreads in the vertical direction, the film cooling effectiveness gradually decreases. Increasing the blowing ration to BR=1 is shown to have a detrimental impact on the film cooling effectiveness as shown in figure 6-14(b), 6-15 and 6-16. As shown in flow visualization, the jet lifts off the surface which explain the decrease in film cooling effectiveness near the hole region. As the jet interacts with the mainstream and the velocity of the jet is reduced, the film cooling effectiveness increases. At the highest blowing ratio of BR=1.5, with the high momentum of the cooling jet and the penetration of the jet into the mainstream, the jet lift-off dominates the surface film cooling effectiveness.

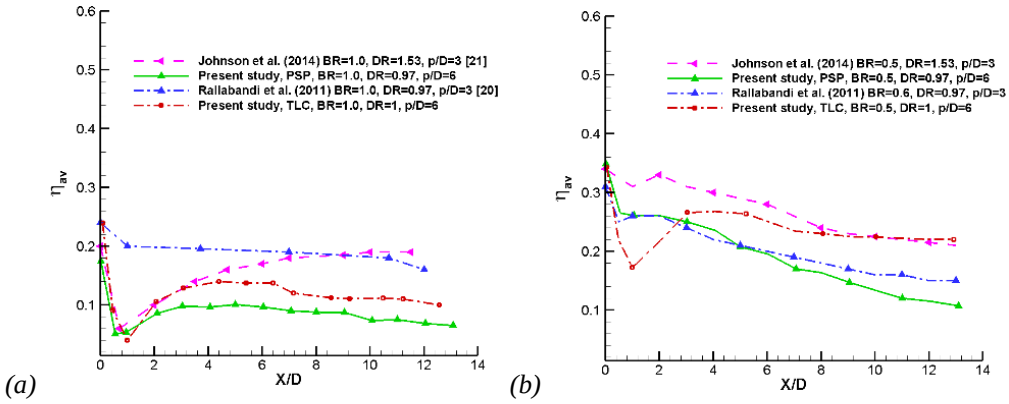

Figure 6-13. Comparison of the laterally averaged cooling effectiveness distribution of present study with literature: (a) BR=0.5; (b) BR=1.

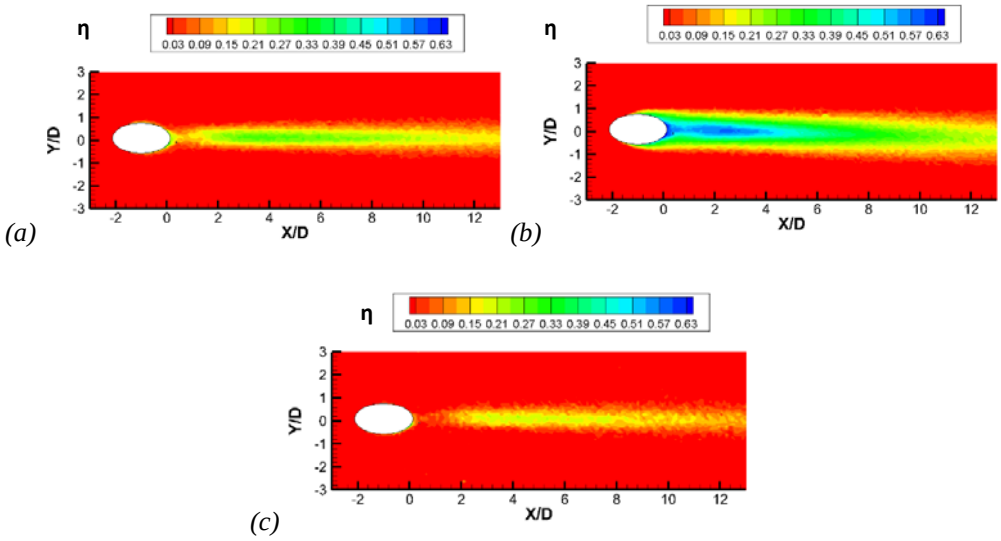

Figure 6-14. Adiabatic cooling effectiveness contours: (a) BR = 0. 5; (b) BR = 1; (c) BR = 1.5.

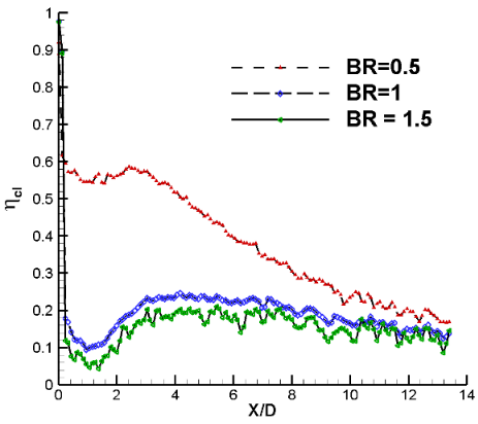

Figure 6-15. Centerline cooling effectiveness profiles.

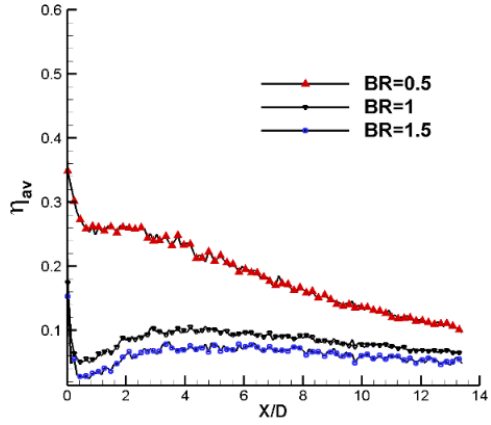

Figure 6-16. Laterally-averaged cooling effectiveness profiles.

Another set of experiments were conducted with CO_2 as coolant stream to measure the film cooling effectiveness on the flat plate surface at closely matched values of blowing ratio, BR, and momentum ratio, I, in order to investigate the density effect on adiabatic film cooling effectiveness as well as assessing the applicability of other scaling quantities such as momentum ratio.

Figure 6-17 compares adiabatic film cooling effectiveness contour for blowing ratio of BR=1 for tests with N_2 and CO_2 as foreign gases considering the same blowing ratio and the same momentum ratio. Besides, Figures 6-18, 6-19 gives the corresponding profiles of the cooling effectiveness along the centerline of the coolant injection hole and the laterally-averaged film cooling effectiveness as a function of the distance away from the coolant injection hole for all three cases.

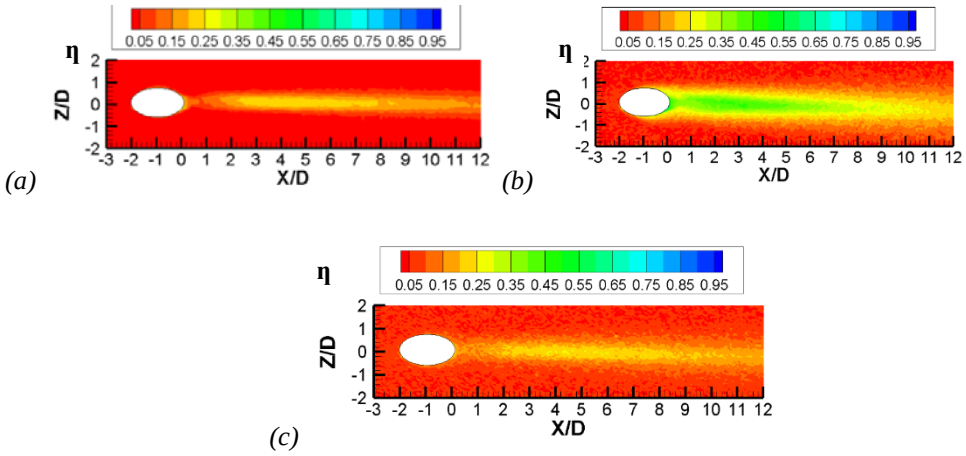

Figure 6-17. Adiabatic cooling effectiveness contours for BR=1: (a) Nitrogen, DR=1; (b) CO_2, DR=1.53, matched blowing ratio; (c) CO_2, DR=1.53, matched momentum flux ratio.

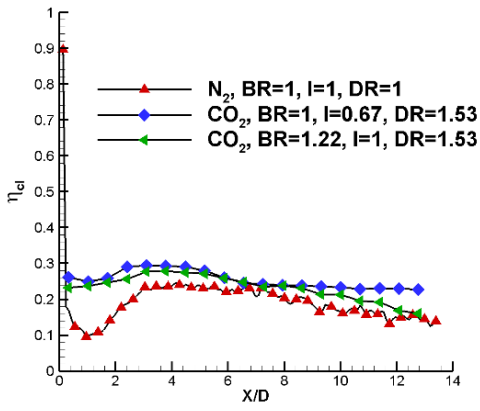

Figure 6-18. Centerline cooling effectiveness profiles for BR=1.

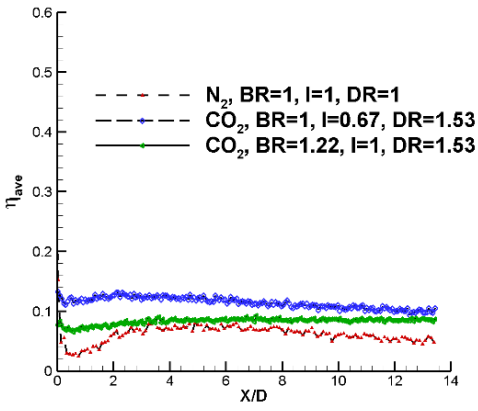

Figure 6-19. Laterally-averaged cooling effectiveness profiles for BR=1.

From figures 6-18 and 6-19, it can be clearly seen that at matched momentum flux ratio, laterally-averaged and centerline cooling effectiveness obtained from either experiment are quite similar, no matter which coolant was used. In addition, considering the same blowing ratio, laterally-averaged and centerline cooling effectiveness of test with CO_2 is greater than a test with N_2 as coolant stream due to higher density ratio of CO_2 with respect to air.

6.1.2 Numerical Result

In the following, simulation predictions obtained from using three different turbulence models were compared to experimental results for cylindrical hole geometry in terms of aerodynamic and thermal parameters at BR=1. In the present work, blowing ratio of unity was chosen for performing simulation since film cooling jet in this blowing ratio detaches from the surface, and then reattaches to the surface and leaves traces of film cooling on the surface. Separation from flat plate surface and penetration of jet into the mainstream make this blowing ratio a challenging condition for performing simulation in comparison with BR=0.5. On the other hand, although in case of BR=1.5 jet separates from a flat plate, it completely loses thermal protection on the surface.

6.1.2.1 Grid sensitivity

A grid sensitivity analysis was performed to ensure the grid size did not influence the simulation results. Table 6-1 is a summary of the meshes used for cylindrical holes. Figure 6-20 shows the result obtained by the three grids for the velocity profile at 5 diameter downstream of injection holes at BR=1.5 as the worst case since at this blowing ratio, as it was concluded from experimental results, jet indicates a strong mixing and high velocity gradient near the hole region in comparison to two other blowing ratios (i.e. BR=0.5, 1).

The RKE model was adopted in the RANS simulations. Good agreement is shown among the numerical results except in the jet core for the coarsest grid. Due to lack of grid cells in the coarse mesh, the flow separation could not be resolved and lower velocity peak was predicted. The medium grid was employed for simulation since similar results are obtained for these two grids.

Table 6-1. Grid sensitivity for cylindrical holes.

Grid	Base Size	Refinement grid size	Cells count
Coarse	0.03	0.001	5,785,194
Medium	0.02	0.0008	9,009,781
Fine	0.02	0.0006	12,567,134

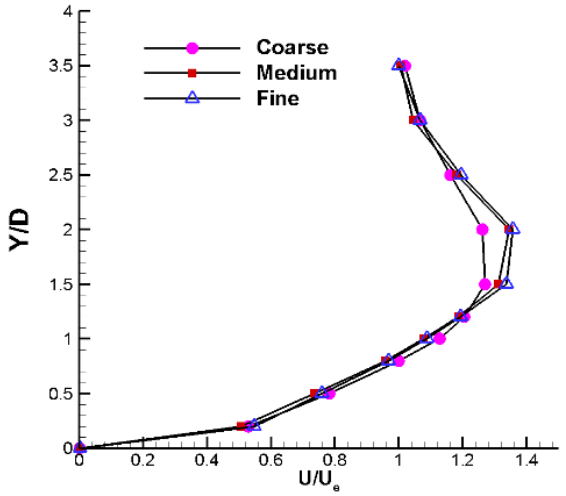

Figure 6-20. Comparison of normalized streamwise velocity profile at X=5D obtained from the different grid.

6.1.2.2 Turbulence Model Selection

Three turbulence models, realizable K-ε, SST K-ω and RSM, are used to investigate the aerothermal behavior of film cooling jet injected from three cylindrical holes at BR=1. Figure 6-21 shows laterally averaged film cooling effectiveness for all three turbulence models compared to results obtained from PSP measurements. The figure clearly shows that the SST KW and RKE models predict laterally-averaged effectiveness most accurately near the hole.

Far from the hole, all turbulence models underpredict the laterally averaged effectiveness. Centerline adiabatic effectiveness for the same blowing ratio is shown in figure 6-22. All three models over-predict the centerline η in the near hole region whereas RKE and SST KW agree well with experiment results downstream of the holes

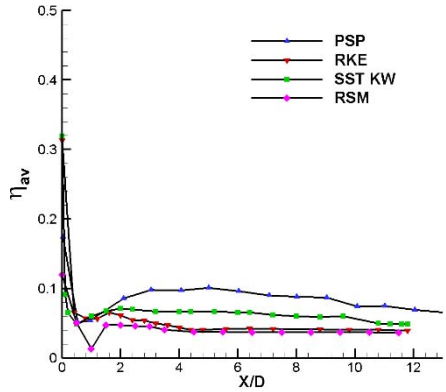

Figure 6-21. Comparison of laterally-averaged effectiveness with experimental data.

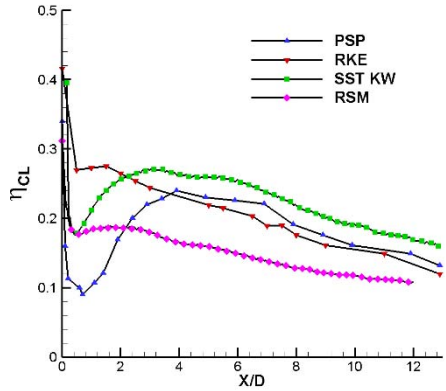

Figure 6-22. Comparison of centerline effectiveness with experimental data.

Figures 6-23 and 6-24 show normalized streamwise velocity profile at 1 and 5 diameter downstream of injection holes and compares the results obtained from the experiment with all three above-mentioned turbulence models. All three turbulence models predict streamwise velocity profile fairly well at X=1D, although SST KW predicts the location of the jet core the best. Further downstream, SST KW model is in best agreement with LDV results comparing to two other turbulence models.

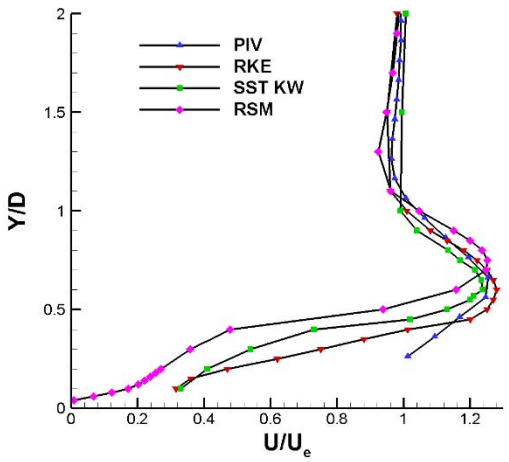

Figure 6-23. Comparison of stream-wise velocity profile with experimental data at X=1D.

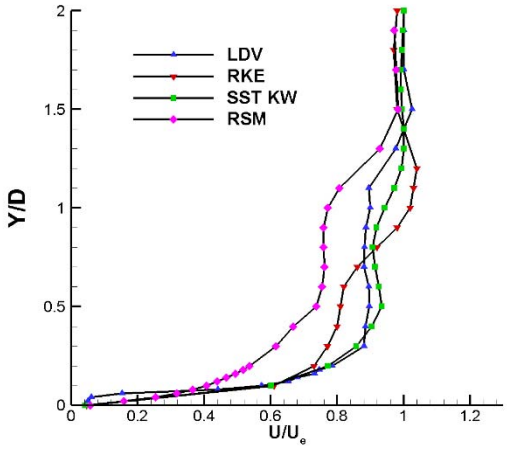

Figure 6-24. Comparison of stream-wise velocity profile with experimental data at X=5D.

Taking into account the comparison of thermal and aerodynamic CFD results with experimental data, one could conclude that the SST KW is the best model to choose for cylindrical holes in these sets of the experiment.

6.1.2.3 Comparison of SST KW with experimental data

Figure 6-25 presents adiabatic film cooling effectiveness contours obtained from PSP measurement and SST KW CFD simulation. The overall features of film cooling effectiveness distribution over flat plate were found to be almost the same in a qualitative sense. However, some minor discrepancies can be identified. For example, near the hole exit, experimental result shows a stronger jet separation than CFD simulation. The contours of film cooling effectiveness obtained from experiment also found to be slightly narrower.

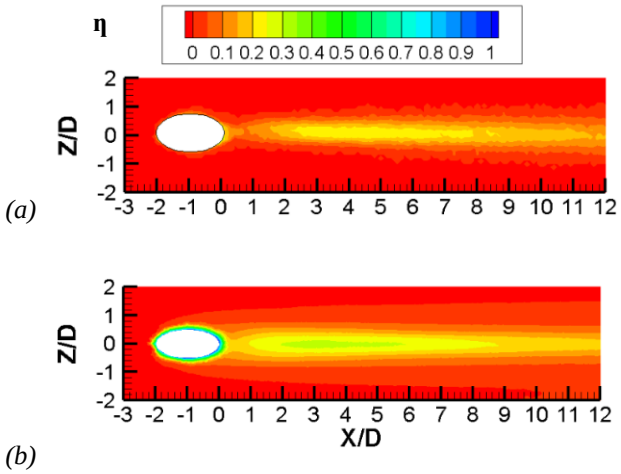

Figure 6-25. Comparison of cooling effectiveness contours with experimental data, (a) PSP; (b) SST KW.

Figure 6-26 (a) shows the contours of normalized velocity in the jet exit plane obtained from SST KW RANS simulation for BR=1. The distribution of velocity at the jet exit is dependent on the blowing ratio and L/D ratio. Since the BR is quite high, it pushes the flow toward the upstream side of the jet exit as it is shown in the figure 6-26 (a). Also, since L/D is high, the separation region has more time to attenuate, and therefore it has less effect on the jet exit condition. Figure 6-26 (b) shows correspondent normalized velocity at the film hole centerline.

From this figure, one could notice that there are different regions in the flow field as Pietzryk et al. [55] documented due to the existence of shear layers downstream of the jet exit along the centerline plane. These regions included the cross flow above the coolant, the coolant jet, the wake region, and the entrained crossflow beneath the coolant.

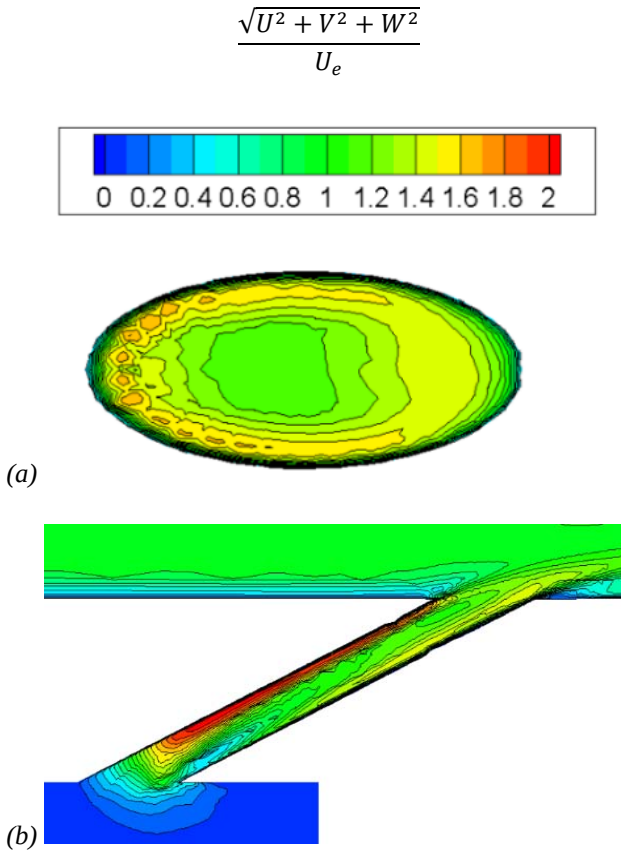

Figure 6-26. Normalized velocity contours, (a) at jet exit plane; (b) at hole centerline.

Figure 6-27 and figure 6-28 compare normalized streamwise and vertical velocity flow field contour obtained from PIV measurements with SST KW CFD simulation, respectively. Both velocity flow field contour match well with CFD simulation.

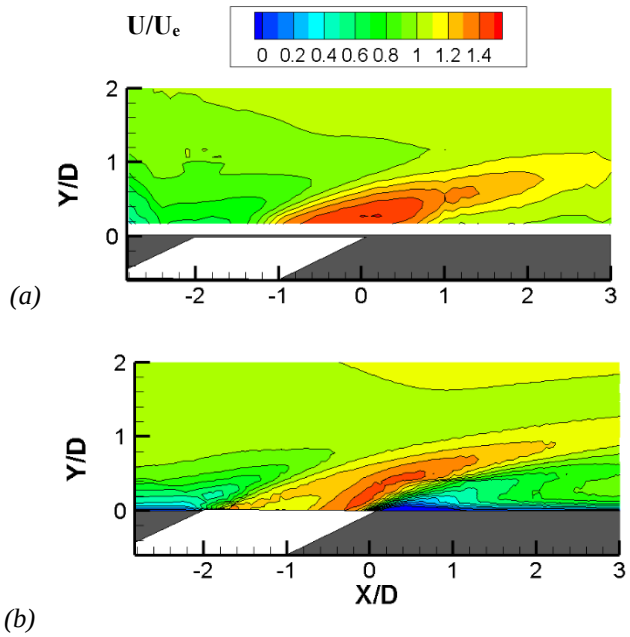

Figure 6-27. Comparison of normalized streamwise velocity contours with experimental data, (a) PIV; (b) SST KW.

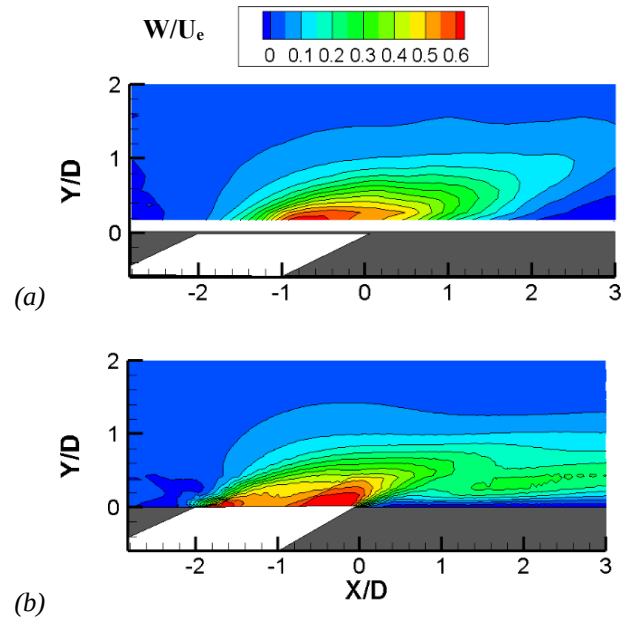

Figure 6-28. Comparison of normalized vertical velocity contours with experimental data, (a) PIV; (b) SST KW.

Figure 6-29 shows the streamwise velocity in a vertical-lateral plane at 1 diameter downstream of the injection hole obtained from hotwire measurements and CFD simulation. Experimental results show stronger penetration of the jet into the mainstream, also jet core happens at the higher elevation relative to the flat plate surface. Also, CFD simulation predicts steeper velocity gradients comparing to experimental result.

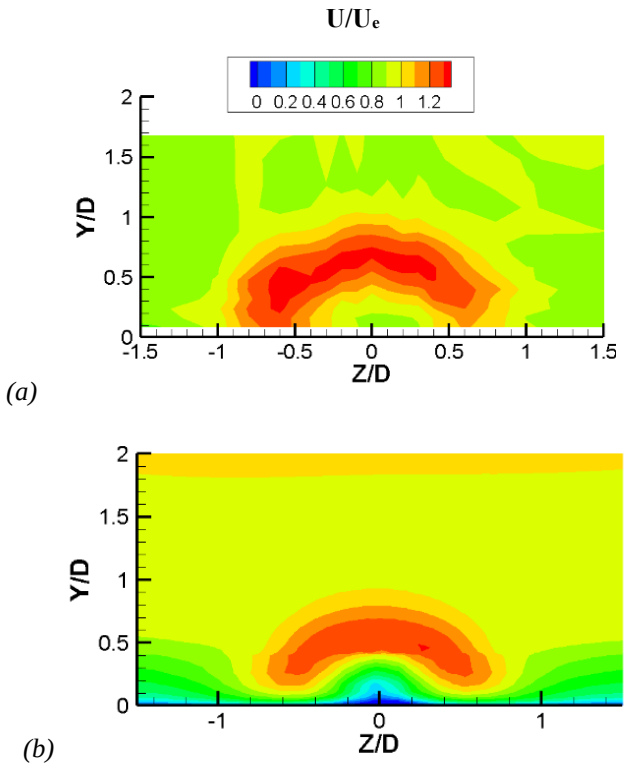

Figure 6-29. Comparison of normalized streamwise velocity contours with experimental data in span-wise plane, (a) HW; (b) SST KW.

6.2 Fan-shaped hole

This section reports the experimental results for fan-shaped holes for BR=1-2 as well as numerical results at BR=1.

6.2.1 Experimental Results

Experimental results include fan-shaped hole characterization, the aerodynamic and thermal behavior of film cooling jet ejected from fan-shaped holes.

6.2.1.1 Discharge Coefficient

The same procedure has been done for fan-shaped holes in order to characterize injection condition. Figure 6-30 shows the C_d distribution versus the ratio of coolant pressure $p_{t,c}$ to the free stream static pressure, p_e . In this case, the ideal mass flow rate is calculated considering the area of a cylindrical hole with the same diameter as the inlet section of the shaped holes.

The discharge coefficient of fan-shaped holes was found to be higher than the cylindrical one, even at lower pressure ratio due to higher pressure recovery. The increment in pressure ratio leads to separation of the flow entering the diffuser from the diffuser wall, thereby reducing the pressure recovery and the discharge coefficient [56].

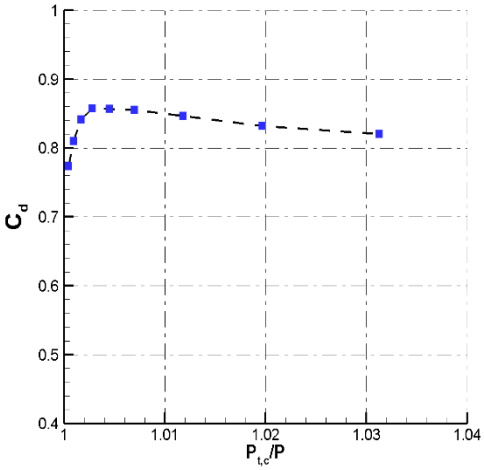

Figure 6-30. Hole Discharge Coefficient.

6.2.1.2 Aerodynamic Survey

Boundary layer profile downstream of the holes at hole centerline

Results from LDV measurements at hole centerline are reported in Figure 6-31 and Figure 6-32 in terms of profiles of time-averaged streamwise velocity component and streamwise and wall normal rms velocities at X/D = 1 and X/D = 5, respectively. Data are normalized with respect to the mainstream velocity U_e. For all blowing ratio, there is no indication of a strong shear layer. Also, the velocity profile is relatively flat downstream of the hole exit. The coolant wake observed in cylindrical hole case is not apparent in this case since the film cooling jet is spread evenly over the test surface.

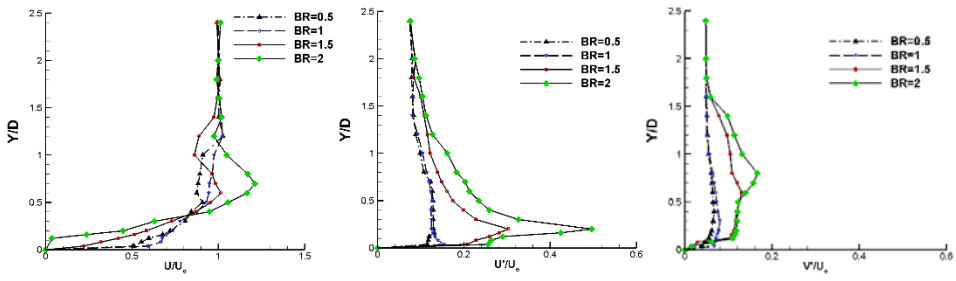

Figure 6-31. Boundary layer Profiles at X/D=1.

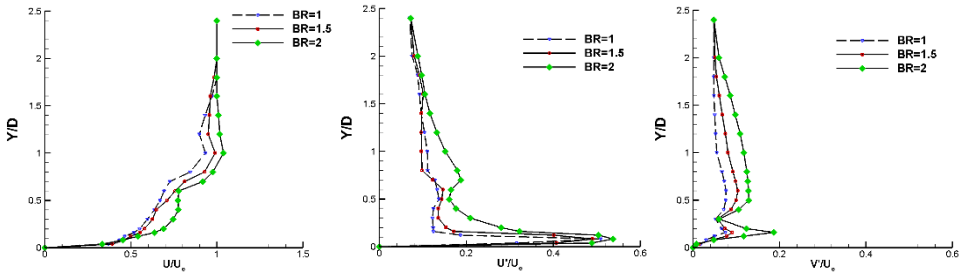

Figure 6-32. Boundary layer Profiles at X/D=5.

2D flow field in (X, Y) plane at Z/D=0

PIV technique was used to characterize the mean and turbulent flow distribution over a 2D plane located at mid hole centerline (Z/D=0). Normalized mean velocity flow fields in the near-hole region for blowing ratio of 1, 1.5 and 2 are shown in figures 6-33. As clearly shown in this figure, for all blowing ratios, the coolant jet stays attached to the surface of the flat plate which is in agreement with LDV results. In contrast to the cylindrical holes, in this case, upward streamline doesn't happen until hole centerline (X/D=-1) which indicates stronger penetration of jet into the mainstream in cylindrical hole case.

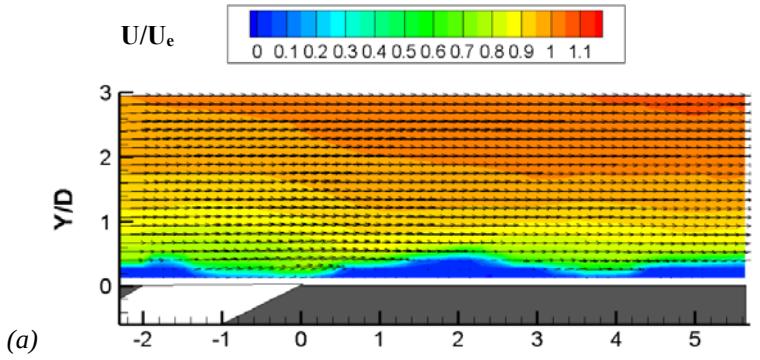

(a)

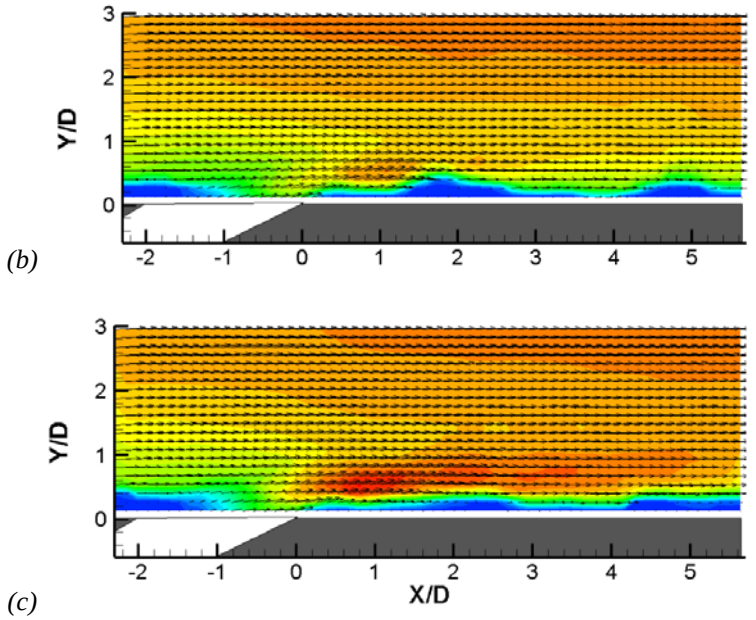

Figure 6-33. Flow Velocity Field at Z/D = 0: (a) BR = 1.0; (b) BR = 1.5; (c) BR = 2.0.

Flow Visualization

To investigate the unsteady behavior of coolant to the mainstream mixing process, flow visualization performed over two planes: (X, Y) and (X, Z) planes. Figure 6-34 depicts flow visualizations for variable injection conditions in the streamwise plane at Z/D=0. For all blowing ratio, coolant jet stays close to the surface and no separation happens near the hole exit. In addition, flow visualization of the coolant jet on the flat plate surface (fig. 6-35) gives rise to the fact that coolant jet spread more laterally over flat plate surface rather than penetrating into the mainstream.

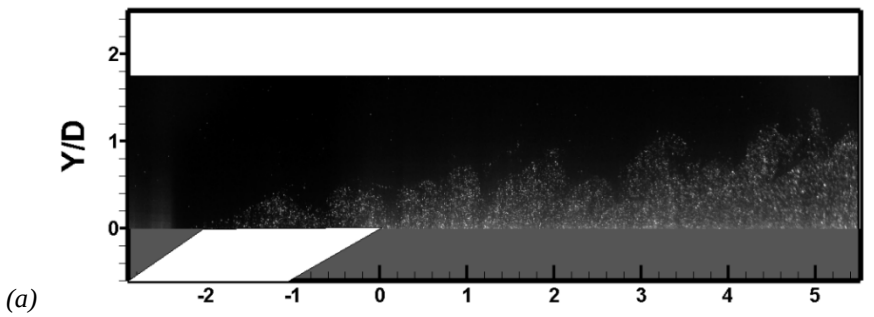

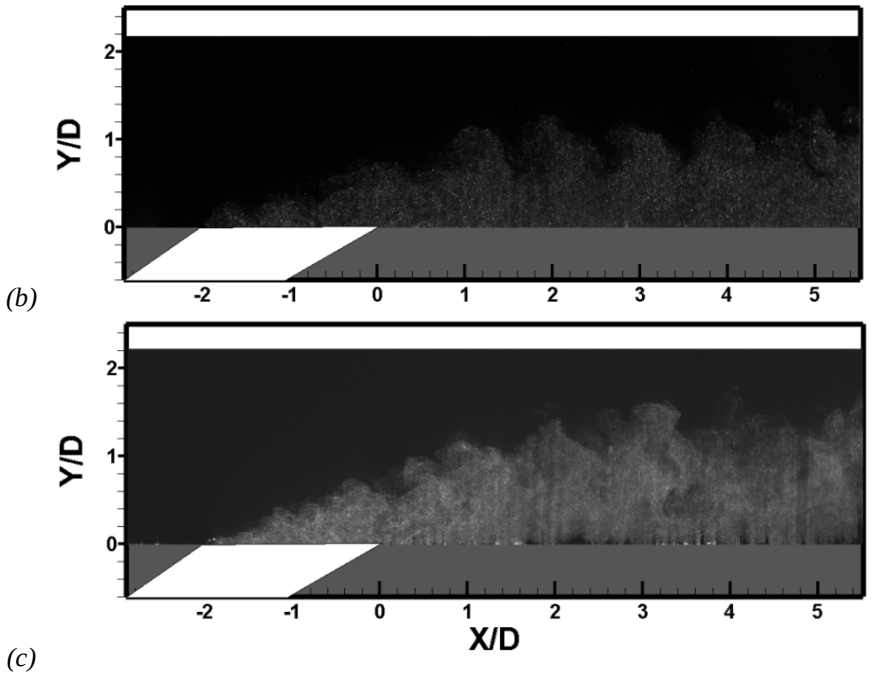

Figure 6-34. Flow Visualization at Z/D = 0: (a) BR = 1.0; (b) BR = 1.5; (c) BR = 2.0.

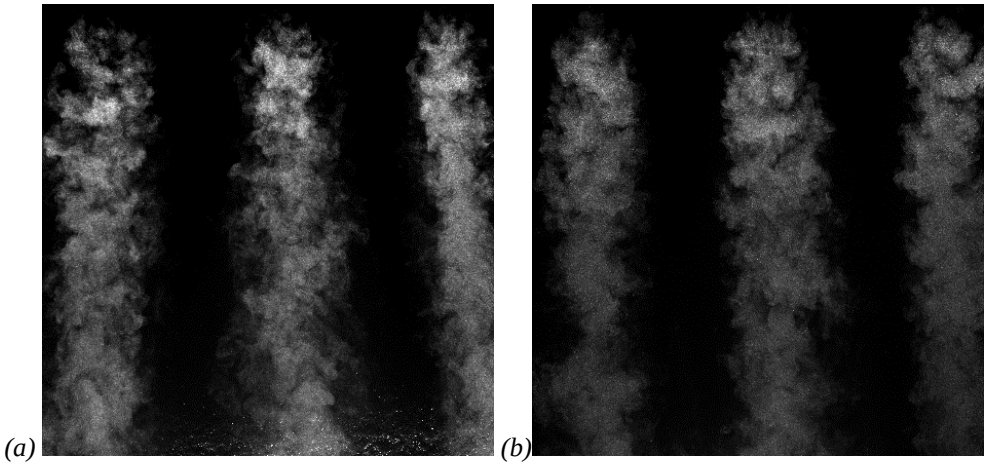

Figure 6-35. Flow Visualization of film cooling jet on flat plate surface: (a) BR = 1.5; (b) BR = 2.0.

2-D flow field in (Y, Z) plane

Hotwire anemometry was used to characterize the coolant to mainstream interaction in (Y, Z) plane at X=1D, X=5D.

❖ Near Field of Jet-Crossflow Interaction

Figure 6-36 shows the stream-wise velocity in a vertical-lateral plane for blowing ratio of BR=1.5, and 2 at 1 diameter downstream of the injection hole. At blowing ratio of BR=1.5, stream-wise velocity contours are relatively uniform, and there is no sign of penetration of jet into the mainstream while at higher blowing ratio jet begin to lift off. Also, the Stronger jet core is noticeable for Blowing ratio BR=2, which is consistent with PIV measurement (Fig. 6-33). Furthermore, near hole region turbulence intensity is about 7% for BR=1.5, whereas, for BR=2, the turbulence intensity peak reaches 10%.

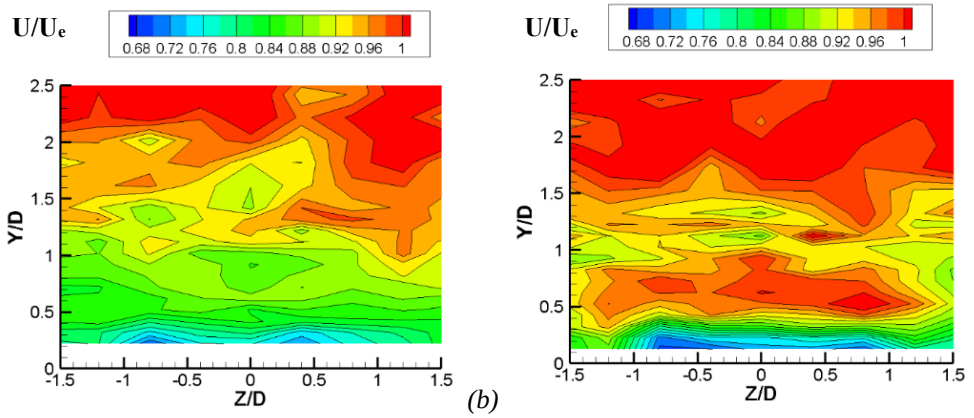

Figure 6-36. Normalized streamwise velocity contours at X=1D: (a) BR = 1.5; (b) BR = 2.0.

❖ Downstream of Jet-Crossflow Interaction

Figure 6-37 shows the streamwise velocity in a vertical-lateral plane for blowing ratio BR=1, 1.5, and 2 at 5 diameter downstream of the injection hole. As jet travel along the flat plate streamwise velocity shows quite similar

behavior for all three blowing ratios. Furthermore, near hole region turbulence intensity is about 5, 6, and 8% for blowing ratio BR=1, 1.5, and 2, respectively.

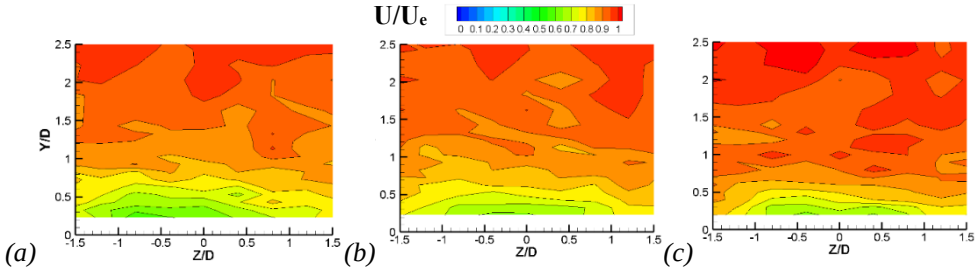

Figure 6-37. Normalized stream wise velocity contours at X=5D: (a) BR = 1.0; (b) BR = 1.5; (c) BR = 2.0.

Comparison LDV- PIV- HW Results

Figures 6-38 shows normalized streamwise velocity profiles for BR=1 obtained from LDV, PIV, and HW measurement techniques at X=5D for fan-shaped hole geometry. As shown in this figure, streamwise velocity profiles obtained from LDV, PIV, and HW measurements are in good agreement and follow the same trend, although the discrepancies could be due to the uncertainty in the position in different measurement techniques.

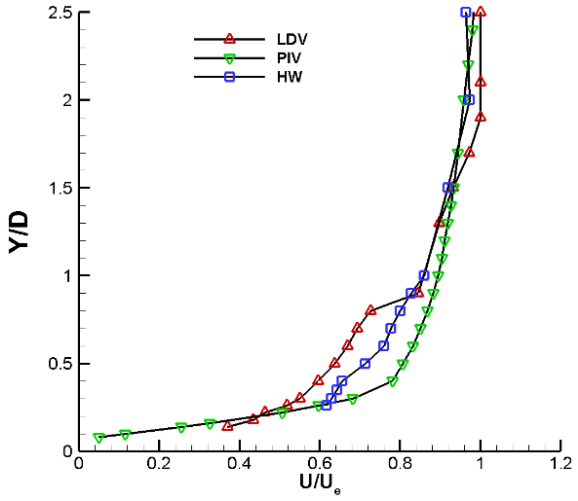

Figure 6-38. Normalized streamwise velocity profiles at X=5D obtained from LDV, PIV, and HW measurement.

6.2.1.3 Thermal Investigation

PSP technique was used to measure adiabatic film cooling effectiveness on the surface of the flat plate. Figure 6-39 shows adiabatic film cooling effectiveness contour for different blowing ratio of BR=0.5, 1, 1.5 and 2, for cases with Nitrogen as coolant stream. For all blowing ratios, the jet attached to the flat plate surface which results in the much better spreading of the jet compared to the cylindrical hole, although for high blowing ratios a small separation zone was found in the vicinity of the hole exit indicated by a slight decrease in effectiveness. Furthermore, Figure 6-40 presents centerline effectiveness as a function of the distance away from the coolant injection hole indicating that the fan-shaped hole provides a high centerline effectiveness yet effectiveness decreases drastically off-centerline.

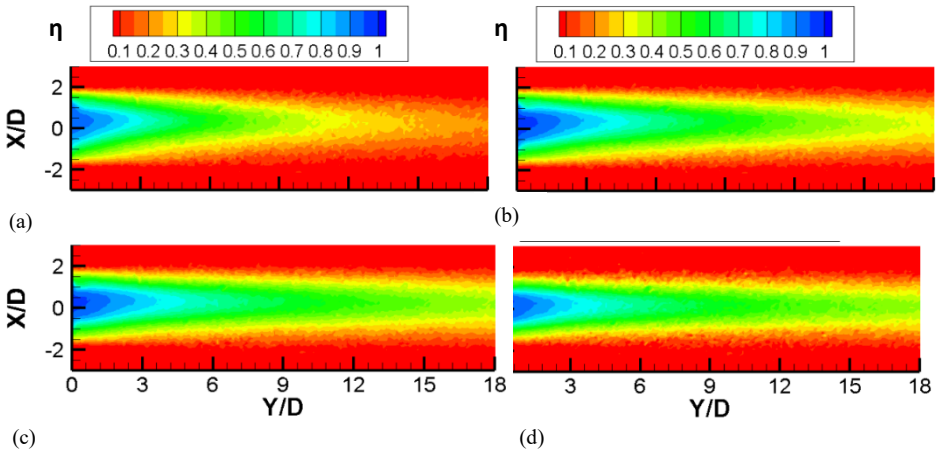

Figure 6-39. Adiabatic cooling effectiveness contours: (a) BR = 0. 5; (b) BR = 1; (c) BR = 1.5; (d) BR = 2.0.

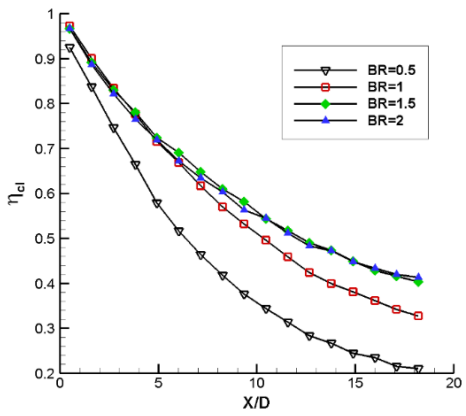

Figure 6-40. Centerline cooling effectiveness profiles.

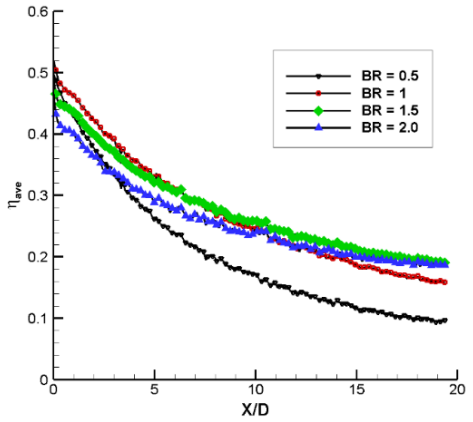

Figure 6-41. Laterally-averaged cooling effectiveness profiles.

Figure 6-41 shows laterally averaged film-cooling effectiveness plotted versus streamwise distance for all four blowing ratios. Effectiveness decreases monotonously with streamwise distance from the hole for all blowing ratios. Maximum effectiveness was found at a blowing ratio of unity. Further increasing the blowing ratio leads only to a slight reduction of effectiveness.

Similar to cylindrical holes case, another set of experiments was conducted with CO_2 as coolant stream to measure the film cooling effectiveness on the flat plate surface at closely matched values of blowing ratios, BR, and momentum ratio, I. Figure 6-42 compares adiabatic film cooling effectiveness contour for blowing ratio of BR=1 for tests with N_2 and CO_2 as foreign gases considering the same blowing ratio and the same momentum ratio. Besides, Figures 6-43 and 6-44 gives the corresponding profiles of the cooling effectiveness along the centerline of the coolant injection hole and the laterally-averaged film cooling effectiveness as a function of the distance away from the coolant injection hole for all three cases. One could conclude that at the same blowing ratio, the film cooling jet with a greater density ratio would provide better film protection over the flat plate surface than that with a lower density ratio. Also, considering measurement results at the matched momentum flux ratio indicates increasing the blowing ratio improve the film cooling effectiveness. This could be due to the fact that the jet is still attached to the surface.

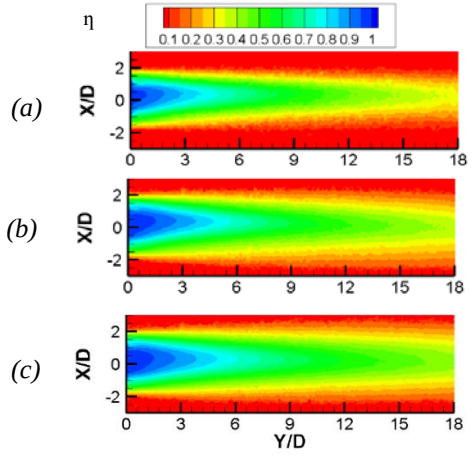

Figure 6-42. Adiabatic cooling effectiveness contours: (a) N_2, BR = 1, I=1, DR=1; (b) CO_2, BR=1, DR=1.53, I=0.65; (c) CO_2, BR=1.237, I=1, DR=1.53.

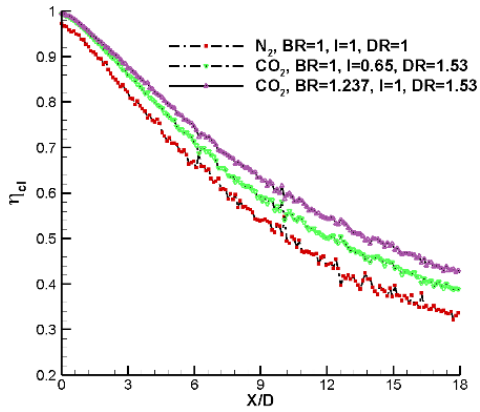

Figure 6-43. Centerline cooling effectiveness profiles.

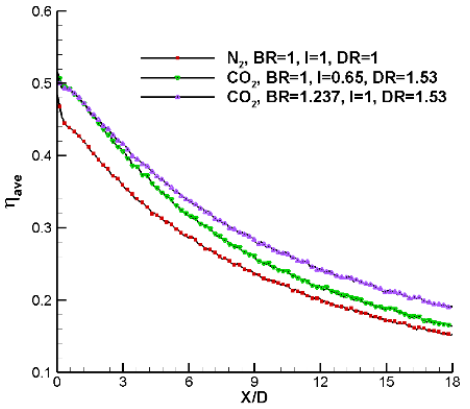

Figure 6-44. Laterally-averaged cooling effectiveness profiles.

Figure 6-45 compares the results of the present study with results of Gritsch et al. [11] at BR=1. Present results are in good agreement with Gritsch results. The differences between data especially near the hole region can be due to larger hole length to diameter ratio of L/D=8 in the present study relative to that of Gritsch et al. (L/D=6).

Trends over the whole range of blowing ratio in both cases are depicted with area-averaged effectiveness plotted in figure 6-46. Area averaging was done from hole trailing edge till 19D downstream of injection hole. Effectiveness increased with blowing ratio up to BR=1 for cases with Nitrogen as coolant stream, whereas cases with coolant with greater density ratio (i.e. CO_2 as foreign gas) the maximum area-averaged effectiveness occurs at higher blowing ratio (i.e. BR=1.5).

Further increase in blowing ratio for both cases leads to narrower effectiveness contours on the surface, and thereby lower area-average effectiveness.

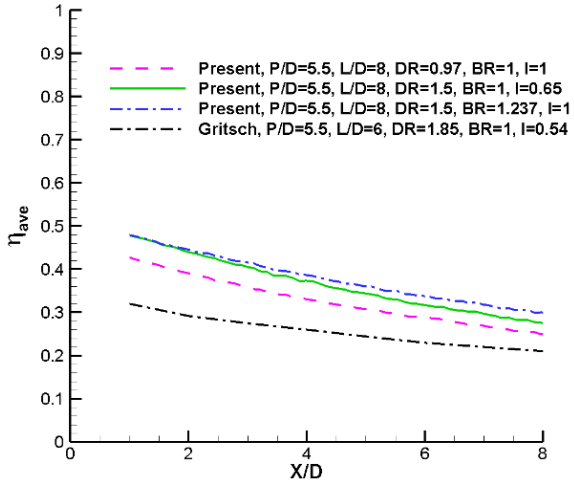

Figure 6-45. Comparison of the laterally-averaged cooling effectiveness distribution of present study with literature.

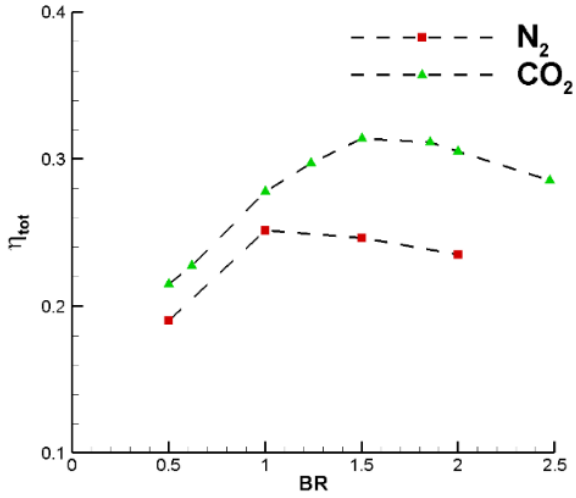

Figure 6-46. Area-averaged cooling effectiveness for N_2 and CO_2.

6.2.2 Numerical Result

In the following, simulation predictions obtained from using three different turbulence models were compared to experimental results for fan-shaped hole geometry in terms of aerodynamic and thermal parameters at BR=1. In the present work, blowing ratio of unity was chosen for performing simulation since this blowing ratio provides optimal adiabatic film cooling effectiveness as well as the best film cooling coverage for fan-shaped hole geometry.

6.2.2.1 Grid Sensitivity

Similar to cylindrical holes case grid sensitivity was performed for fan-shaped holes as well. Table 6-2 is a summary of the meshes used for this case. Figure 6-47 shows the result obtained by two grids (i.e. medium and fine meshes) for the velocity profile 5 diameter downstream of injection holes at BR=1. The RKE model was adopted in the RANS simulations. Good agreement is shown among the numerical results. Though the number of cells is quite different between these two grids, similar results are obtained. From Figure 6-47 the medium grid is found to be optimal, hence the medium one was employed for all the RANS simulations.

Table 6-2. Grid sensitivity for fan-shaped holes.

Grid	Base Size	Refinement grid size	Cells count
Medium	0.02	0.001	6,785,194
Fine	0.02	0.0008	10,920,371

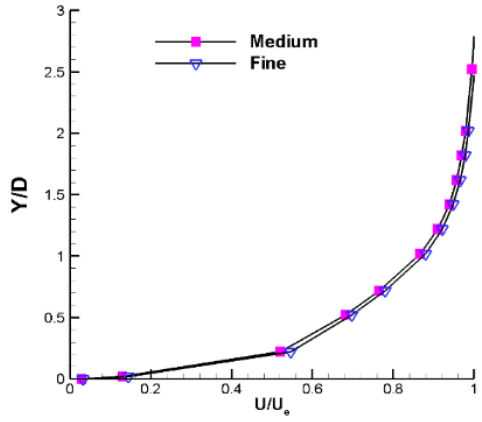

Figure 6-47. Comparison of normalized streamwise velocity profile at X=5D obtained from

6.2.2.2 Turbulence Model Selection

The same procedure has been done for a fan-shaped hole in order to select the best turbulence model that predicts the jet behavior. Figure 6-48 shows laterally-averaged film cooling effectiveness for all three turbulence models compared to results obtained from PSP measurements for BR=1. RSM and RKE models overpredict laterally-averaged effectiveness while SST KW under predicts it. Centerline adiabatic effectiveness for the same blowing ratio is shown in figure 6-49. The figure clearly shows that the RSM and RKE models predict centerline effectiveness the best whereas SST KW predicts centerline effectiveness the worst.

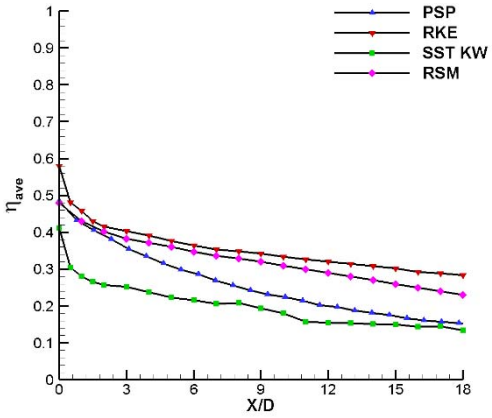

Figure 6-48. Comparison of laterally-averaged effectiveness with experimental result

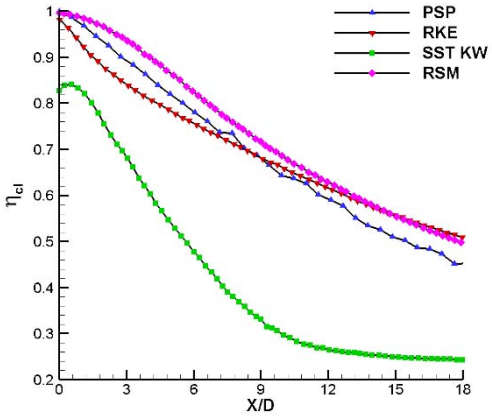

Figure 6-49. Comparison of centerline effectiveness with experimental result

Figures 6-50 shows normalized streamwise velocity profile at 1 and 5 diameter downstream of injection holes and compares the results obtained from the experiment with all three above-mentioned turbulence models. RSM turbulence model predicts streamwise velocity profile the most accurate among other models at X=1D and X=5D.

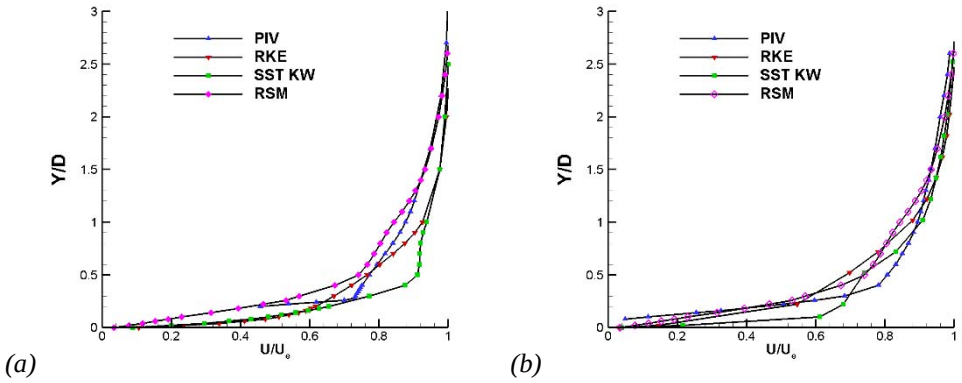

Figure 6-50. Comparison of normalized streamwise velocity with experimental result, (a) X=1D; (b) X=5D.

Figure 6-51 shows normalized vertical velocity profile at 5 diameter downstream of injection holes and compares the results obtained from the experiment with all three above-mentioned turbulence models. Although all three turbulence models underpredict the vertical velocity close to the wall, RSM turbulence model comes closest to the experimental data in this region.

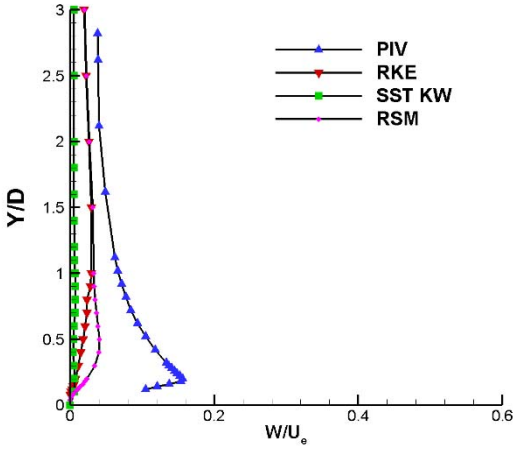

Figure 6-51. Comparison of normalized vertical velocity with experimental result.

Taking into account comparison of thermal and aerodynamic results with CFD simulation, one could conclude that the RSM is the best model to choose for fan-shaped holes in this set of experiments.

6.2.2.3 Comparison of RSM with experimental data

Figure 6-52 presents adiabatic film cooling effectiveness contours obtained from PSP measurement and RSM CFD simulation. As can be seen in this figure, qualitatively, simulation results are in agreement with the experimental result.

Figure 6-53(a) shows the contours of normalized velocity in the jet exit plane obtained from RSM RANS simulation for BR=1. Figure 6-53(b) shows the correspondent normalized velocity at the film hole centerline. The flow smoothly spreads towards the film hole area change and begins to slow as the area is widened which results in much smaller velocity ratio at the hole exit. At the exit plane, a smoother and less severe pressure gradient exists, thereby forming a much less severe blockage than cylindrical holes as it is shown in figure 6-53(b).

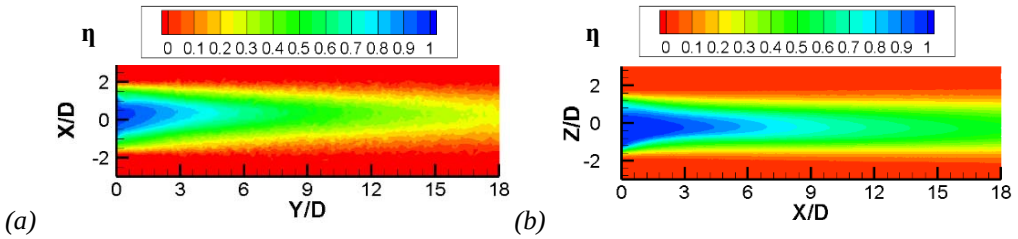

Figure 6-52. Comparison of cooling effectiveness contours with experimental data, (a) PSP; (b) RSM.

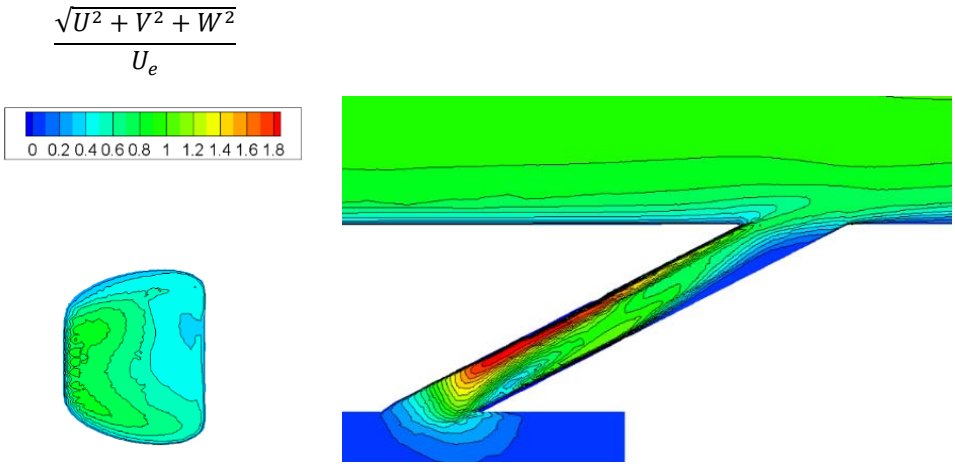

Figure 6-53. Normalized velocity contours, (a) at jet exit plane; (b) at hole centerline.

Figure 6-54 and figure 6-55 present normalized streamwise and vertical velocity flow field contour obtained from PIV measurements and RSM CFD simulation. Both velocity flow field contour match well with CFD simulation.

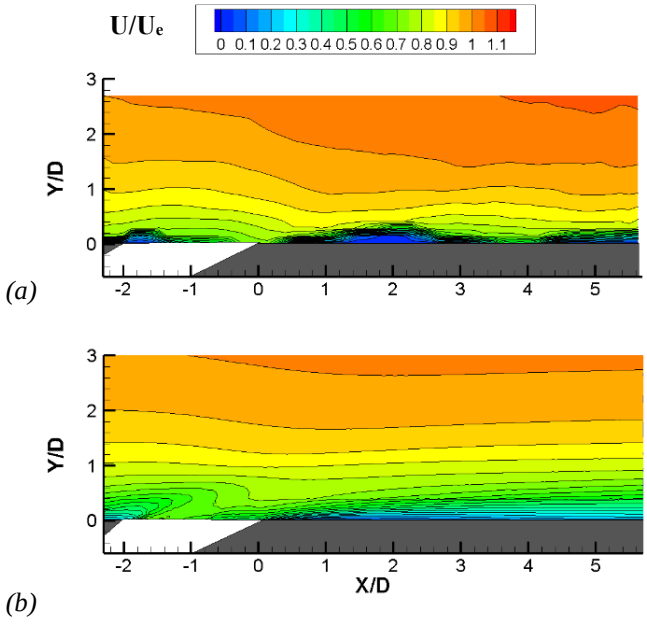

Figure 6-54. Comparison of normalized streamwise velocity contours with experimental data, (a) PIV; (b) RSM.

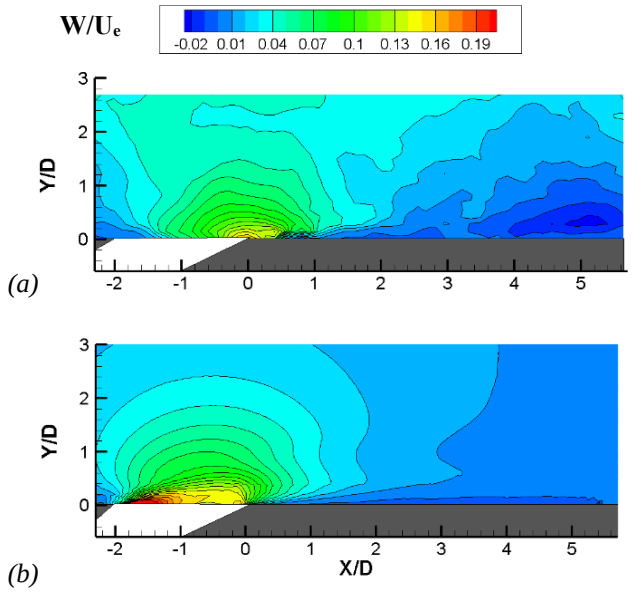

Figure 6-55. Comparison of normalized vertical velocity contours with experimental data, (a) PIV; (b) RSM.

Figure 6-56 shows the streamwise velocity in a vertical-lateral plane at 5 diameter downstream of the injection hole obtained from hotwire measurements and CFD simulation. Hotwire measurement are in good agreement with CFD simulation. However, it seems that RSM model overpredicts jet spreading in the span-wise direction comparing to hotwire result, close to the wall.

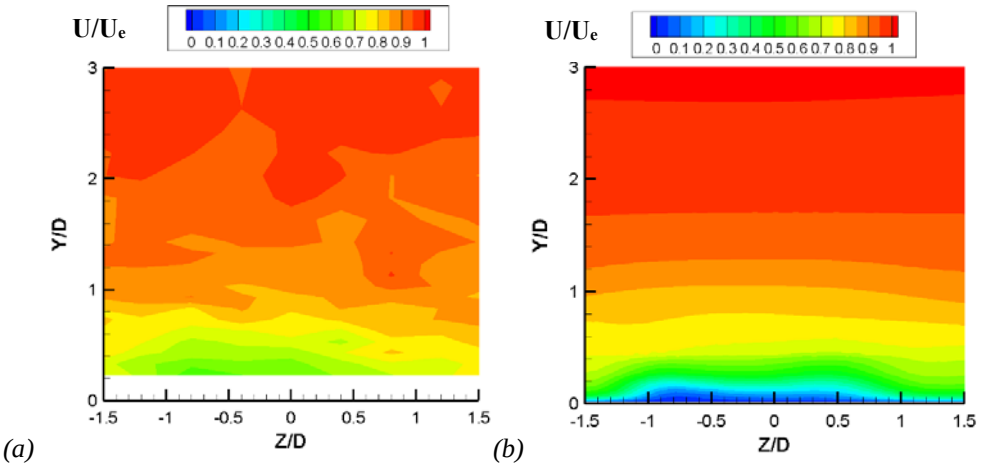

Figure 6-56. Comparison of normalized streamwise velocity contours with experimental data in span-wise plane, (a) HW; (b) RSM.

The normalized stress profiles along the jet center plane (Z/D=0) are presented in Figures 6-57 at *X/D* = 1 and *X/D* = 5, respectively. It could be clearly seen from figure 6-57, Reynolds stress turbulence model predicts the experimental trend of stress components accurately. However, it gives low levels of streamwise stress component close to the wall.

The level of the individual normal stresses in the RSM models are controlled by their respective production terms, the pressure-strain correlation terms and the dissipation rate correlation. As documented by Tyagi et al. [57], the failure of RSM models to capture the experimental trends specifically in the wake of the jet is largely due to under predicted production levels.

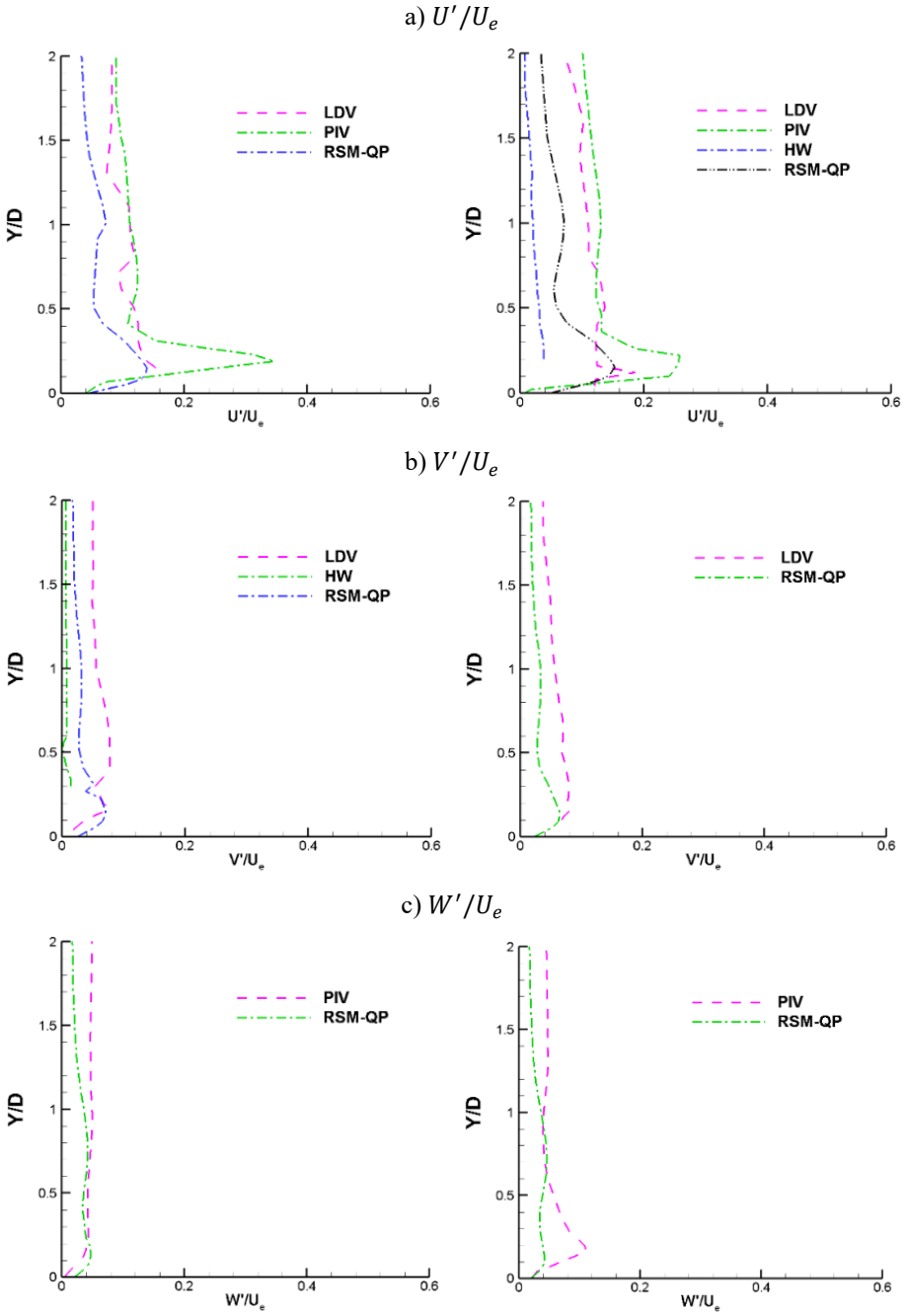

Figure 6-57. Comparison of stress profiles with experimental data at X/D=1, 5 (Z/D=0).

6.3 Influence of Density Ratio

In this section, in order to verify the validity of heat and mass transfer analogy, the prediction of adiabatic cooling effectiveness was carried out using two approaches: the first approach consider a temperature differential between the hot mainstream (T_∞)and the coolant(T_c), and the second approach consider that "hot" mainstream has a gas concentration of C_∞, and the coolant gas has a tracer concentration of C_c . If the turbulent lewis number, Le_T, is equal to 1, heat and mass transfer analogy is valid and therefore the adiabatic cooling effectiveness could be written as follows:

$$\eta = \frac{C_w - C_\infty}{C_C - C_\infty} \approx \frac{T_{aw} - T_\infty}{T_C - T_\infty} \qquad \textit{Equation 6-2}$$

Figure 6-58 compares the CFD predicted results considering these two approaches with PSP results at a density ratio of DR=1.53 for cylindrical holes configuration at BR=1.

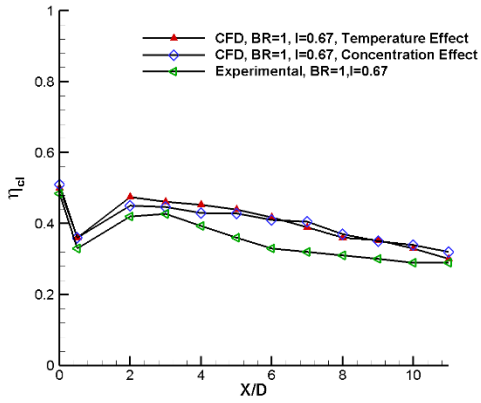

Figure 6-58. Centerline adiabatic effectiveness for DR=1.53 at BR=1

As shown in figure 6-58, predicted centerline η from both computational approaches are the same. However, computational results are slightly greater than experimental results. This difference in η value could be due to the assumption that was made regarding density ratio: i.e. DR considered to be 1 for computational study while in the real case DR is less than 1(DR=0.93). Figure 6-59 shows a comparison between the predicted and measured result of laterally-averaged effectiveness distribution at DR=1.53. It can be clearly seen that PSP results are in agreement with both computational approaches.

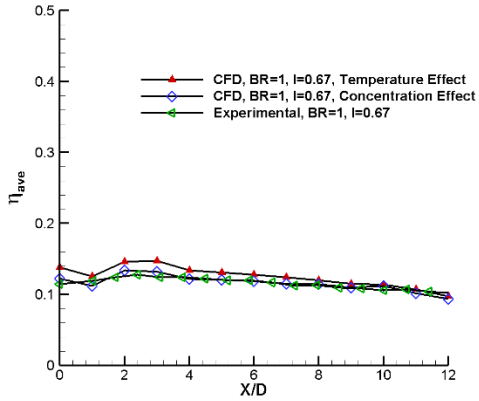

Figure 6-59. Laterally-averaged adiabatic effectiveness for DR=1.53 at BR=1

Finally, to complete computational studies, the influence of density ratio was investigated considering the momentum flux ratio (I=1) instead of Blowing ratio. Results were reported in terms of centerline and laterally-averaged adiabatic effectiveness (Figure 6-60, Figure 6-61).

As can be seen in these figures, at high blowing ratio (BR=1.22) due to jet detachment and reattachment, the simulation over-predicted η near the hole and the agreement between the predicted and measured results became better as the jet reattached to the wall surface.

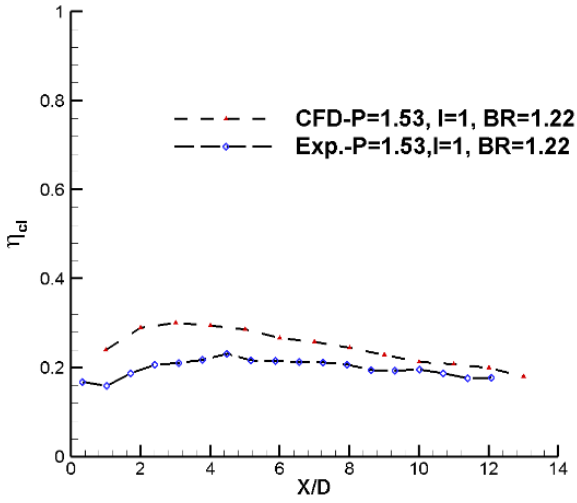

Figure 6-60. Centerline adiabatic effectiveness for DR=1.53 at I=1

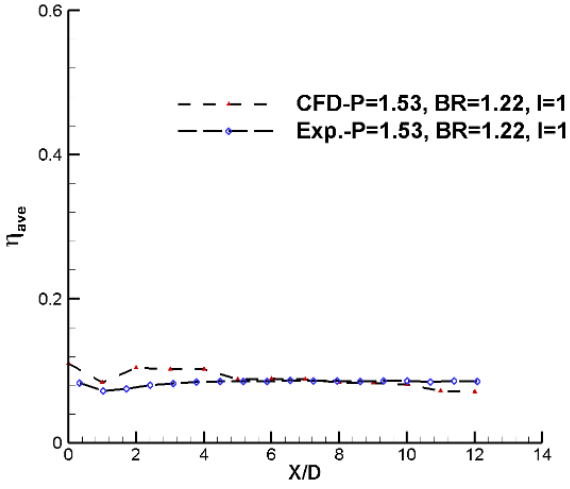

Figure 6-61. Laterally-averaged adiabatic effectiveness for DR=1.53 at I=1

7 CONCLUSIONS

The focus of this thesis was to investigate the interaction between film cooling jet ejected from two different hole geometries (i.e. Cylindrical and fan-shaped hole) and mainstream in terms of aerodynamic and thermal aspects of film cooling using a flat plate wind tunnel with low freestream turbulence intensity. Then, data collected by means of fluid dynamic techniques such as PIV, and PSP have been used to validate numerical studies in order to find the best turbulence models for the closure of steady RANS simulation. Therefore, three turbulence models including RKE, SST KW, and RSM were examined in STAR-CCM$^+$ code and compared with experimental data. The aim was to determine the best turbulence model for predicting laterally and centerline adiabatic effectiveness and velocity flow fields for both investigated hole geometries.

First of all, flow fields and adiabatic film cooling effectiveness for a row of three cylindrical holes have been measured at blowing ratio of BR=0.5-1.5. 2-D flow field measurements at streamwise plane have shown that jet stays attached to the flat plate surface at blowing ratio less than 1, while for cases with blowing ratio greater than 1 coolant jet lifts off the flat plate surface. Furthermore, flow visualizations have shown the presence of large coherent structures at the jet boundaries for both hole geometries. In addition, 2-D flow

field measurement at vertical-lateral plane indicates the presence of kidney vortices at 1 diameter downstream of injection holes which becomes negligible as jet travels along the flat plate due to mixing between jet and mainstream. Thermal measurements besides 2-D flow field measurements give a complete picture of jet structure in the crossflow. As centerline and laterally averaged adiabatic film cooling effectiveness have been shown, no detachment and reattachment have been observed for BR=0.5, while at BR=1 the jet attached and reattached to the surface of flat plate. Increasing the BR to 1.5 leads to the complete loss of thermal protection on the flat plate surface. Furthermore, in order to investigate the effect of density ratio on adiabatic film cooling effectiveness, another set of experiments were conducted with CO_2 as coolant stream. It could be concluded that the use of the coolant stream with density ratio greater than 1 (in this case CO_2), would result in increased cooling effectiveness over the tested surface. Then, detailed experimental data was used to validate three different turbulence models in STAR-CCM$^+$ code at BR=1. This study has shown that SST KW is the best choice for cylindrical holes for prediction of adiabatic effectiveness as well as velocity flow fields.

Second of all, flow fields and adiabatic film cooling effectiveness measurements were repeated for a row of three fan-shaped holes at various coolant blowing ratio of BR=1-2. 2-D flow field measurements at streamwise plane have shown that the velocity profile is relatively flat downstream of the hole exit for all blowing ratios, and the coolant jet stays attached to the surface. 2-D flow field measurement at vertical-lateral plane indicates no sign of penetration of jet into the mainstream until blowing ratio 2. From thermal measurement, one could draw a conclusion that effectiveness decrease monotonously with streamwise distance from the hole for all blowing ratios. Maximum effectiveness was found at a blowing ratio of unity. Further increasing the blowing ratio leads only to a slight reduction of effectiveness. Moreover, in case of using a coolant stream with density ratio higher than 1,

the maximum effectiveness occurs at BR=1.5. Examination of three different turbulence model for the fan-shaped hole at BR=1 results in the selection of RSM turbulence model to provide closure for RANS simulation in terms of aerodynamic and thermal parameters.

From the aerodynamic and thermal point of view, comparison of cylindrical and fan-shaped holes leads to these conclusions:

- From the aerodynamic point of view, the jet penetration, as well as the velocity gradients were significantly reduced for the laterally expanded holes relative to cylindrical one. Furthermore, hotwire measurements indicate no strong vortical motion in the vertical-lateral plane in case of fan-shaped holes.
- Thermal results have indicated that by laterally expanding the exit of the hole, higher effectiveness values could be obtained over a wide range of blowing ratios which could be explained by reduced velocity gradient as well as the uniform and smooth penetration at X/D=5.

Finally, the analogy between the heat and mass transfer was numerically validated, showing that the adiabatic cooling effectiveness obtaining from mass transfer and heat transfer approaches were in agreement.

To wrap it up, the collected data could be a useful database for unsteady as well as advanced hybrid URANS-LES CFD simulations for future works.

NOMENCLATURE

Notation	Description
q	Heat Transfer Between Film Cooling Jet and Blade Surface
h	Heat Transfer Coefficient
T_f	Film Cooling Temperature
T_w	Blade Surface Temperature
η	Adiabatic Film Cooling Effectiveness
T_∞	Hot Gas Temperature
T_{aw}	Adiabatic Wall Temperature
T_c	Coolnt Temperature
D	Hole Diameter
α_c	Injection Angle
P	Hole Pitch
L	Hole length
DR	Density Ratio
Tu	Turbulence Intensity, %
U',V', W'	Root-mean-squre Velocity Components
U_e	Mainstream Velocity
BR	Blowing Ratio
ρ_c	Coolant Density
ρ_∞	Mainstream Density
u_c	Coolant Velocity
I	Momentum Flux Ratio
δ	Boundary Layer Thickness
Ma_{is}	Isentropic Mach Number
ɣ	Specific Heat Ratio
P_t	Total Pressure
P_0	Static Pressure
R	Gas Constant
I_w	Hot wire Probe Current
Re	Reynolds Number
X,Y, Z	Cartesian Coordinate System
$\boldsymbol{\lambda}$	Turbulent Length Scale
C_d	Discharge Coefficient
δ*	Displacement Thickness
H_{12}	Shape Factor
U, V, W	Velocity Components
y^+	Dimensionless Wall Distance
k	Turbulent Kinetic Energy
ε	Turbulent Kinetic Energy Dissipation Rate
ε_{ij}	dissipation tensor

μ_t	Turbulent Viscosity
$\overline{u_i' u_j'}$	Reynolds Stresses
δ_{ij}	Kronecker delta
μ	Dynamic viscosity
ϑ	Kinematic viscosity
α	Thermal Diffusivity
ϕ_{ij}	Pressure-strain Correlation
ω	Specific Turbulence Dissipation Rate
Le_T	Turbulent Lewis Number
C_∞	Mainstream Concentration
C_c	Coolant Concentration

ACRONYMS

Notation	Description
RANS	Reynolds Average Navier Stokes
LES	Detached Eddy Simulation
DES	Detached Eddy Simulation
DNS	Direct Numerical Simulation
SKE	Standard k-ε
SW	Standard Wall Function
2LWT	Two Layer Wall Treatment
RNG	Renormalization Group k-ε
RSM	Reynold's Stress Models
SST	Shear Stress Transport
SKW	standard k-ω
SST KW	Menter SST k-ω
PIV	Particle Image Velocimetry
HWA	Hotwire Anemometry
PSP	Pressure Sensitive Paint
TLC	Thermo Liquid Crystal
LDV	Laser Doppler Velocimetry
CTA	Constant temperature anemometers

REFERENCES

[1] M.M. El-Wakil, Power Plant Technology.

[2] Han, J. C., Dutta, S., Ekkad, S. V., 2000, "Gas Turbine Heat Transfer and Cooling Technology", Taylor & Francis.

[3] Sautner, M., Clouser, S., Han, J.C., 1993, "Determination of Surface Heat Transfer and Film Cooling Effectiveness in Unsteady Wake Flow Condition", AGARD Conference Proceedings 527.

[4] Halila, E. E., Lenahan, D. T., Thomas, T. T., "Energy Efficient Engine", GE Co., NASA CR-167955.

[5] Moustapha, H., Zelesky, M. F., Baines, N. C., Japikse, D. "Axial and Radial Turbines" Concepts NREC, 2003.

[6] Goldstein, R.J., 1971, "Film Cooling," Advances in heat transfer, 7, 321-379.

[7] Han, J. C., Ekkad, S. V., 2001, "Recent Development in Turbine Blade Film Cooling," International Journal of Rotating Machinery, 7(1), 21-40.

[8] Bogard, D., and Thole, K., 2006, "Gas Turbine Film Cooling," Journal of Propulsion and Power, 22(2), 249-270.

[9] Bunker, R., 2005, "A Review of Shaped Hole Turbine Film Cooling Technology," Journal of Heat Transfer, 127, 441.

[10] Ligrani, P. M., Lee, J. S., 1996, "Film Cooling from a Single Row of Compound Angle Holes at High Blowing Ratios," International Journal of Rotating Machinery, Vol. 2, pp. 259-267.

[11] Gritsch, M., Schulz, A., and Wittig, S., 1998, "Adiabatic Wall Effectiveness Measurements of Film-cooling Holes with Expanded Exits", Journal of Turbomachinery, 120, 549.

[12] Lutum, E., and Johnson, B. V., 1999, "Influence of the Hole Length to-Diameter Ratio on Film Cooling With Cylindrical Holes." ASME Journal of Turbomachinery 121: 209-216.

[13] Goldstein, R.J., Eckert, E.R.G., and Burggraf, F., 1974, "Effects of Hole Geometry and Density on Three Dimensional Film Cooling," International Journal of Heat and Mass Transfer, 17(5), 595-607.

[14] Sinha, A. K., Bogard, D., and Crawford, M., 1991,"Film Cooling Effectiveness Downstream of a Single Raw of Holes with Variable Density Ratio," Journal of Turbomachinery, 113(3), 442-449.

[15] Rallabandi, A.P., Li, S.J., and Han, J.C., 2010, "Unsteady Wake and Coolant Density Effects on Turbine Blade Film Cooling Using PSP Technique," Proc. ASME IMECE, Heat Transfer Division, HTD, Chicago, IL, United States.

[16] Ligrani P.M., Wigle J.M., Ciriello S., Jackson S.M., "Film Cooling from Holes with Compound Angle Orientations: Part 1- results downstream of holes with 3d span-wise spacing," ASME J Heat Trans 1994; 116(2):341-52.

[17] Ahn J, Jung I.S., Lee J.S., "Film Cooling from Two Rows of Holes with Opposite Orientation Angles: Injectant Behavior and adiabatic film cooling effectiveness." International Journal of Heat Fluid Flow, 2003, 24(1):91-9.

[18] Kusterer, K., Bohn, D., Sugimoto, T., and Tanaka, R., 2007,"Double-Jet Ejection of Cooling Air for Improved Film Cooling," Journal of Turbomachinery, 129(4), 809-815.

[19] Saumweber, C., Schulz, A., and Wittig, S., 2003, "Free-stream Turbulence Effects on Film-Cooling with Shaped Holes," Journal of Turbomachinery, 125, PP. 65-73.

[20] Jumper, G. W., Elrod, W. C., and Rivir, R. B., 1991, "Film Cooling Effectiveness in High Turbulence Flow," Journal of Turbomachinery, 113, PP.479-483.

[21] Stefan H., 2007, "Unified Turbulence Models for LES and RANS, FDF and PDF Simulations," Theoretical and Computational Fluid Dynamics, Vol. 21, pp. 99-118.

[22] Walters D.K., and Leylek J.H., 1997,"A Systematic Computational Methodology Applied to a Three-dimensional Film Cooling Flow field," Journal of Turbomachinery, v119, p777-785.

[23] Ferguson, J.D., Walters D.K., and Leylek J.H., 1998, "Performance of Turbulence Models and Near Wall Treatments in Discrete Jet Film Cooling Simulations," ASME Paper 98-GT-438.

[24] Walters D.K., and Leylek J.H., 2000, "A Detailed Analysis of Film Cooling Physics: Part 1- Streamwise Injection with Cylindrical Holes," Journal of Turbomachinery, v122, p 102-112.

[25] Javadi, A., Javadi, K., Taeibi-Rahni, M., Keimasi, M.R., 2002, "Reynold's Stress Turbulence Models for Prediction of Shear Stress terms in Cross Flow Film Cooling Numerical Simulation," PVP2002-1586, Computational Technologies for Fluid/Thermal/Structural/Chemical Systems with Industrial Applications, v 2, P 155-167.

[26] Ajersch, P., Zhou, J.M., Ketler, S., Salcudean, M., Gartshore I.S., 1995, "Multiple Jets in a Crossflow: Detailed Measurements and Numerical Simulations," ASME Paper 95-GT-9.

[27] York W.D., and Leylek J.H., 2003, "Three-dimensional Conjugate Hear Transfer Simulation of an Internally-cooled Gas Turbine Vane," ASME Paper GT2003-38551.

[28] Hylton, L.D., Milhec, M.S., Turner, E.R., Nealy D.A., York, R.E., 1983,"Analytical and Experimental Evaluation of Heat Transfer Distribution Over the Surface of Turbine Vanes," NASA CR 168015.

[29] Silieti, M., Divo, E., Kassab A.J., 2 004,"Numerical Investigation of Adiabatic and Conjugate Film Cooling Effectiveness on a Single Cylindrical Film-cooling Hole," ASME Paper IMECE2004-62196.

[30] Hassan, J.S., Yavuskurt, S., (2006), "Comparison of Four Different Two-equation Models of Turbulence in Predicting Film Cooling Performance," ASME Paper GT2006-90860.

[31] Gustafsson, K.M.B., Johansson, T.G., 2006, "Numerical Simulation of Effusion Cooling with Comparison to Experimental Data," Progress in Computational Fluid Dynamics, v6, n 1/2/3, p 101-109.

[32] Harrison, K.L., Bogard, D.G., "Comparison of RANS Turbulence Models for Prediction of Film Cooling Performance", ASME GT2008-51423, pp. 1187-1196

[33] Silieti, M., Kassab, A.J., and Divo, E., 2005, "Film cooling effectiveness from a single scaled-up fan-shaped hole a CFD simulation of adiabatic and conjugate heat transfer models," ASME Paper GT2005-68431.

[34] Fawcett, R.J., Wheeler, A.P.S., He, L., Taylor, R. 2010, Experimental Investigation into Unsteady Effects on Film Cooling, In Proceedings of the ASME Turbo Expo, Glasgow, GT2010-22603.

[35] Barigozzi, G., Ravelli, S., Armellini, A., Mucignat, C., Casarsa, L., 2013, Effects of Injection Conditions and Mach Number on Unsteadiness Arising Within Coolant Jets Over a Pressure Side Vane Surface, Int. J. of Heat and Mass Transfer 67, p 1220–1230.

[36] Adrian, R.J., "Twenty Years of Particle Image Velocimetry. Experiments in Fluids," 39(2):159-169, July 2005.

[37] Raffel, M., Willert, C., Wereley, S.T., and Kompenhans, J., “Particle Image Velocimetry: a practical guide,” Springer-Verlag Berlin Heidelberg, Berlin, Germany, 2007.

[38] M. Manshadi, B. Keshavarz, M. Soltani and K. Ghorbanian, "An innovative genetic algorithm approach for direct calibration of X-probe hot wires," Experimental Techniques, vol. 36, no. 1, pp. 50-60, 2012.

[39] J. Moro, P. Vukoslavcevic and V. Blet, "A method to calibrate a hot-wire X- Probe for applications in low-speed, variable-temperature flow," Measurement Science and Technology, vol. 14, pp. 1054-1062, 2003.

[40] M. Hultmark and A. Smits, "Temperature corrections for constant temperature and constant current hot-wire anemometers," Measurement Science and Technology, vol. 21, 2010.

[41] M. Ndoye, J. Delville, D. Heitz and G. Arroyo, "Parameterizable constant temperature anemometer: a new method for the analysis of velocity-temperature coupling in turbulent heat transfer," Measurement Science and Technology, vol. 21, 2010.

[42] M. T. Wylie, A. W. Brown and B. G. Colpitts, "Distributed hot-wire anemometry based on Brillouin optical tim-domain analysis," Optics Express, vol. 20, no. 14, pp. 15669-15678, 2012.

[43] ISSI, 2015, Binary FIB Pressure Sensitive Paint, Innovative Scientific Solutions, Inc., Dayton, OH, http://www.psp-tsp.com/.

[44] Zhang L.J., Fox M., “Flat Plate Film Cooling Measurement Using PSP and Gas Chromatograph Techniques,” ASME Paper AJTE99-6241 1999.

[45] Jones T V. Theory for the Use of Foreign Gas in Simulating Film Cooling. Int. J. Heat Fluid Flow 1999; 20(3):349–354.

[46] Han J-C, Rallabandi AP. Turbine Blade Film Cooling Using PSP Technique. Front. Heat Mass Transfer 2010; 1: 1–21.

[47] Natsui G et al. A Detailed Uncertainty Analysis of Adiabatic Film Cooling Effectiveness Measurements Using Pressure-Sensitive Paint. J. Turbomach. 2016; 138(8):081007.

[48] Foroutan, H., Yavuzkurt, S., 2015, Numerical Simulation of the Near-Field Region of Film Cooling Jets Under High Free Stream Turbulence: Application of RANS and Hybrid URANS/Large Eddy Simulation Models, Journal of Heat Transfer 137(1) 011701.

[49] CD-Adapco, STAR-CCM+ Users Guide, v9.06.

[50] Launder, B. E., and Spalding, D. B., 1974, "The Numerical Computation of Turbulent Flows," Computer Methods in Applied Mechanics and Engineering, Vol. 3, pp. 269-289.

[51] Menter, F. R, 1994, Two-Equation Eddy-Viscosity Turbulence Models for Engineering Applications. *AIAA Journal*, 32(8):1598-1605.

[52] Lien, F. , and Leschziner, M., 1994, "Assessment of turbulence-transport models including non-linear RNG eddy-viscosity formulation and second-moment closure for flow over a backward facing step," Computers Fluids, vol. 23, no. 8, pp. 983-1004.

[53] Speziale, C. G., Sarkar, S. and Gatski, T. B., 1991, "Modeling the pressure-strain correlation of turbulence: All invariant dynamical systems approach," d. Fluid Mech., Vol. 227, pp. 245-272.

[54] Gritsch, M., Schulz, A., Wittig, S., "Discharge Coefficient Measurements of Film-cooling Holes with Expanded Exits," 1998, Journal of turbomachinery, Vol. 120 (3), pp. 557-563.

[55] Pietrzyk, J. R., Bogard, D. G., Crawford, M. E., "Hydrodynamic Measurements of Jet in Crossflow for Gas Turbine Film cooling Applications," 1989, Journal of turbomachinery, Vol. 111 (2), pp. 139-145.

[56] Hay, N., Lampard, D., "Discharge Coefficient of Turbine Cooling Holes: A Review," 1998, Journal of turbomachinery, Vol. 120 (2), pp. 314-319.

[57] Hoda, A., Acharya, S., Tyagi M., "Reynolds Stress Transport Model Predictions and Large Eddy Simulation for Film Coolant Jet In Cross Flow," 2000, Heat Transfer; Electric Power; Industrial and Cogeneration, Vol. 3.

[58] Barigozzi, G., Franchini, G., Perdichizzi, A., "The Effect of An Upstream Ramp on Cylindrical and Fan-shaped Hole Film Cooling-Part I: Aerodynamic Results," ASME Turbo Expo 2007: Power for Land, Sea, and Air, Vol. 4, pp. 105-113.

[59] Barigozzi, G., Franchini, G., Perdichizzi, A., "The Effect of An Upstream Ramp on Cylindrical and Fan-shaped Hole Film Cooling-Part I: Adiabatic Effectiveness Results," ASME Turbo Expo 2007: Power for Land, Sea, and Air, Vol. 4, pp. 115-123.

[60] Yavuzkurt, S., Hassan, J., S., "Evaluation of Two-equation Models of Turbulence in Predicting Film Cooling Performance Under High Freestream Turbulence," ASME Turbo Expo 2007: Power for Land, Sea, and Air, Vol. 4, pp. 259-268.

[61] Wright, L.M., McClain, S.T., and Clemenson, M.D., 2011, "Effect of Freestream Turbulence on Film Cooling Jet Structure and Surface Effectiveness Using PIV and PSP," ASME Journal of Turbomachinery, Vol. 133, No 4, Article 041023, 12 pages.

[62] Wright, L.M., McClain, S.T., and Clemenson, M.D., 2011, "Effect of Density Ratio on Flat Plate Film Cooling with Shaped Hole Using PSP," ASME Journal of Turbomachinery, Vol. 133, No 4, Article 041011 , 11 pages.

[63] Voigt, S., Noll, B., Aigner, M., "Aerodynamic Comparison and Validation of RANS, URANS, and, SAS Simulation of Flat Plate Film-

Cooling", 2010, ASME Journal of Turbomachinery, Vol. 4, pp. 1471-1480.

[64] Vinton, K., R., Watson, T., B., Wright, L.M., Crites, D., C., Morris, M., C., Riahi, A., "Combined Effects of Freestream Pressure Gradient and Density Ratio on the Film Cooling Effectiveness of Round and Shaped Holes on a Flat Plate", 2016, ASME Journal of Turbomachinery, 041003, 10 Pages.